Nonlinear two-dimensional wing control based on inverse method

CHENXI ZHANG

School of Aeronautic Science and Engineering, Beihang University, Beijing, China
JIAYING ZHANG

School of Aeronautic Science and Engineering, Beihang University, Beijing, China

Abstract—A flutter suppression strategy based on the inverse dynamic method is proposed for a two-degree-of-freedom (2-DOF) wing section equipped with trailing-edge (TE) and leading-edge (LE) control surfaces. A smooth reference trajectory is constructed to guide the plunge and pitch degrees of freedom from a perturbed state back to the equilibrium position. The inverse dynamic method is then employed to track this trajectory, thereby achieving flutter suppression in simulation. The stability of the closed-loop system is analyzed using Lyapunov stability theory under stated assumptions. For the nonlinear problems in 2-DOF wing systems, three nonlinear pitch stiffness forms in the wing system are studied. In addition, the Monte Carlo method is used to solve the uncertainty problems in this nonlinear system and to obtain the flutter failure probability distribution at different freestream velocities. For this wing system, the controllable boundary is defined as the freestream velocity at which the cumulative probability of closed-loop flutter occurrence reaches 0.1%. This controllable boundary can be predicted via the Monte Carlo method. The discrete and continuous gust models are also established for wind gusts that the wing may encounter. The inverse dynamic method is shown to control the system acceleration responses into a small range under the proposed gust disturbance.

Keywords: Active flutter suppression, 2-DOF wing section, Inverse method, Parameter uncertainty, Gust alleviation

1 Introduction

One of the future trends in the design of modern aircraft structures is the increasing structural flexibility, which may lead to complex aeroelastic instability risks. In flight, the interaction between the structure, inertia and aerodynamic forces may cause self-excited vibrations such as flutter [1][2].

Authors' address: C. X. Zhang and J. Y. Zhang are with the School of Aeronautic Science and Engineering, Beihang University, Beijing 102206, China, E-mail: (zy2305423@buaa.edu.cn; jiaying.zhang@buaa.edu.cn). (*Corresponding author: Jiaying Zhang.*)

The flutter phenomenon can lead to the critical damage to the structure of the flight vehicle, and is detrimental to flight safety. Various flutter suppression methods have emerged with the in-depth study of these problems. According to different principles, the overall techniques can be divided into passive and active flutter suppression (AFS) [3]. The main measures of the former include: (1) Changing the local or global stiffness of the structure [4]. (2) Placing masses at predefined locations to eliminate inertial or aerodynamic coupling. Despite the high safety and reliability of the method, it leads to increased weight, reduced performance and higher system structure costs. To address the deficiencies of the passive flutter suppression method, the AFS technique has rapidly appeared and developed since the 1970s [3]. After decades of research, AFS technology has matured and has been successfully applied to the X-56A Unmanned aerial vehicle (UAV) [5].

At the same time, the development of modern control theory [6] has led to advancements in control system design from single-input/single-output (SISO) to multiple-input/multiple-output (MIMO). It has provided an abundant theoretical foundation for AFS technology. For linear SISO/MIMO system, traditional control methods such as proportional integral derivative (PID) [7], linear quadratic regulation (LQR) [8] and linear quadratic gaussian (LQG) [9], have been effective and easy to implement. However, the aeroelastic problems of the wing system often exhibit nonlinearity, making linear control methods unsuitable. Such nonlinearities are caused by factors like worn hinges on control surfaces, gaps in the control surfaces, nonlinear material properties and various other factors [10][11]. Additionally, uncertainties resulting from design, manufacture, assembly and measurement of the wing structures make it challenging to describe them quantitatively [12][13].

The uncertainty of the system has an important impact on the aeroelastic problem. Li and Yang [12] studied the influence of uncertainties in a 2-DOF wing section with free play stiffness, using Monte Carlo simulation (MCS) and Gaussian random variables to quantify the uncertainties in the flutter problem. Wu and Livne [13] developed a similar Monte Carlo framework and showed that aerodynamic damping uncertainty dominates flutter prediction for the AGARD test wing. In practice, manufacturing tolerances and measurement inaccuracies introduce further parametric uncertainties. Recent tools such as interval-theory-based data-driven identification [14], panel/boundary-layer coupled aerodynamic analysis [15], and LES-based forced-vibration studies [16] have improved uncertainty quantification and flow prediction. However, these methods either treat the system as a black box or focus primarily on the flow physics, without separating the compensation of known nonlinear dynamics from the treatment of residual uncertainties. A systematic decoupling of nominal nonlinearity cancellation from offline uncertainty quantification, as proposed in this work, has not been addressed in these studies.

In addition to parametric uncertainties, aircraft structures are subjected to gust disturbances during flight, which poses a further challenge for control design [17][18]. Reliable gust alleviation therefore requires accurate characterization of the gust environment and precise response prediction. Recent studies on dynamic coverage control in time-varying wind fields [19] and wavelet-based multi-horizon trajectory prediction [20] show that refined environmental modelling improves prediction fidelity. These works, however, do not address the direct cancellation of structural nonlinearities, which is the core of the present control strategy. It should also be noted that structural vibration can be mitigated through passive damping mechanisms, such as the memory effects of viscoelastic and thermoelastic materials [21-24]. While these approaches provide an alternative path for vibration reduction, they rely on material energy dissipation rather than active control of the aeroelastic dynamics.

In recent years, several control algorithms have been developed for the aircraft or wing model systems, including sliding mode control (SMC) [25][26], robust and fault-tolerant control [27-29], adaptive control [30][31], active disturbance rejection control (ADRC) [32-34], and active dynamic vibration absorbers [35]. Li et al. [26] proposed an observer-based SMC strategy for high-dimensional bending-torsion coupling flutter with delayed output, achieving effective suppression using piezoelectric patch actuators. However, the control law relies on a discontinuous switching mechanism, which may excite unmodelled high-frequency structural modes. Schmidt et al. [29] used robust H_∞, modal isolation and damping for adaptive aeroelastic suppression (MIDAAS) and identically located acceleration and force (ILAF) to suppress body-freedom flutter (BFF) on a test-bed aircraft, treating the nonlinear pitch stiffness as model uncertainty bounded by frequency-domain weighting functions. Yang et al. [33] proposed an error-based control law using the ADRC algorithm to remove the flutter instability for a 2-DOF wing model with measurement noise and uncertain parameters. In this framework, the stiffness is absorbed into the total disturbance estimated and compensated by the extended state observer. In both approaches, the nonlinear stiffness is not directly cancelled in the control law but is instead handled indirectly as an uncertainty or disturbance. Mozaffari-Jovin et al. [31] proposed an L_1 adaptive controller for an unsteady flapped airfoil, and demonstrated effective flutter suppression. In this framework, the closed-loop transient response is governed by a linear reference model, and the aeroelastic states follow the dynamics of that model rather than an explicitly planned trajectory from the perturbed state to the equilibrium. Ebrahimzadeh et al. [35] proposed an active dynamic vibration absorber (ADVA) for a 2-DOF wing model, with feedback gains optimised by a genetic algorithm. The active absorber further extended the flutter boundary and exhibited robustness to parameter variations. This strategy suppresses flutter by modifying the equivalent damping and stiffness of the system, without prescribing an explicit reference trajectory for the plunge and pitch responses.

As a further comparison, several advanced control strategies achieve robustness by explicitly incorporating uncertainties online. Examples include distributed fault-tolerant formation control with prescribed performance [36], neural-network-based sliding mode control for quadrotors [37], and event-triggered predefined-time attitude control for spacecraft [38]. In contrast, the proposed inverse dynamic approach analytically cancels the nominal nonlinearity and assigns uncertainty quantification to an offline Monte Carlo assessment. This decoupling avoids introducing additional conservatism into the online loop while providing a probabilistic stability boundary.

Unlike existing studies, this paper proposes a novel flutter suppression strategy based on the inverse dynamic method. The inverse dynamic method utilizes differential geometric analysis to achieve exact linearization of nonlinear systems and systematic control law design [39][40]. It has been widely applied to trajectory tracking problems, including robot manipulator control [41], satellite attitude maneuvers [39], aircraft and missile guidance [42][43], and vehicle trajectory optimization [44]. These applications demonstrate its flexibility in path planning, computational efficiency, and ability to meet prescribed boundary conditions. Despite these advantages, the inverse dynamic method typically relies on a predefined external reference trajectory. Consequently, this method is not directly applicable to stabilization problems, such as flutter suppression. In flutter suppression, the primary objective is to eliminate the vibrations in both the plunge and pitch degrees of freedom, thereby driving the system from a perturbed position to the equilibrium position. Nevertheless, there exists no such predefined reference trajectory that can smoothly accomplish this transition. To address this, this paper proposes a method to generate such a smooth, continuous trajectory from the perturbed position to the equilibrium position. The inverse dynamic method is then employed to force the time-domain responses of both degrees of freedom to track this trajectory. In this manner, the flutter of the 2-DOF wing system can be effectively suppressed through the proposed control strategy.

Compared with the existing flutter suppression strategies reviewed above, the proposed method differs in three fundamental aspects. First, a smooth reference trajectory is explicitly planned for the suppression transient, rather than leaving the response to be shaped indirectly by feedback gains or absorber dynamics. Second, the nonlinear pitch stiffness is cancelled analytically through the inverse dynamics control law, instead of being treated as a disturbance or uncertainty to be rejected or adapted to. Third, nonlinearity compensation and uncertainty quantification are decoupled. The nominal nonlinear terms are cancelled directly in the control law, while parametric uncertainties are quantified offline via the Monte Carlo method. This decoupling provides a probabilistic stability boundary and avoids introducing conservatism into the online controller. The same framework is further extended to gust load alleviation, covering both discrete and continuous gust scenarios.

The contributions of this paper are:

Contribution 1: A novel control strategy for suppressing 2-DOF wing flutter based on the inverse dynamic method is proposed. By constructing the reference trajectory internally through linearization and LQR, this strategy extends the classical inverse dynamics method from trajectory tracking to the stabilization of self-excited vibrations.

Contribution 2: A decoupled treatment is established whereby nominal nonlinearities are cancelled analytically in the control law while parametric uncertainties are quantified offline via the Monte Carlo method. The closed-loop controllable boundary, defined at a cumulative flutter probability of 0.1%, is obtained under Gaussian parameter uncertainties.

Contribution 3: The inverse dynamic method is extended to gust load alleviation under both discrete 1-cosine and continuous gusts, with alleviation performance quantified via root-mean-square acceleration reduction rates.

The rest of this paper is as follows. The Section 2 conducts modeling of a 2-DOF wing system with nonlinear pitch stiffness. The Section 3 introduces the flutter control scheme based on the inverse dynamic method. The Section 4 conducts numerical simulations for active flutter control of this system. The Section 5 investigates the closed-loop controllable boundaries of flutter with parameter uncertainty. The Section 6 applies this control scheme to gust load alleviation. The Section 7 is the conclusion.

2 Nonlinear aeroelastic model

This paper investigates a classical two-dimensional wing section with LE and TE control surfaces, as shown in Fig. 1. Platanitis and Strganac [45] previously investigated this model's performance though both experiments and simulation studies. It is evident that this system has 4 degrees of freedom. However, as the high frequency dynamics of LE and TE control surfaces are significantly different from the 2-DOF plunge and pitch wing system, only the latter are considered in the dynamic equations. The inertia and stiffness properties of the control surfaces are ignored, focusing solely on their effect on aerodynamic forces. The variables in this paper are named in TABLE I.

TABLE I System parameters nomenclature

Symbol	Meaning	Symbol	Meaning
b	semi-chord of wing section	C_l	wing section lift coefficient
a	non-dimensional distance from mid-	C_m	wing section moment coefficient at

	chord to elastic axis		quarter-chord
x_α	non-dimensional distance from elastic axis to center of mass	$C_{l\alpha}$	$\partial C_l/\partial \alpha$ ($C_{l\beta}$, $C_{l\gamma}$, $C_{m\alpha}$, $C_{m\beta}$, $C_{m\gamma}$) have the similar definitions
s	wing section span	c_h	plunge damping
m_{W}	mass of wing section	c_α	pitch damping
m_{T}	total mass of pitch–plunge system	k_h	plunge stiffness
I_α	total mass moment of inertia about elastic axis	k_α	pitch stiffness
h	plunge displacement	L	aerodynamic lift
α	pitch angle	M	aerodynamic moment
β	trailing edge control surface deflection	σ	standard deviation
γ	leading edge control surface deflection	μ	average value
U	freestream velocity	C_v	σ/μ , coefficient of variation
ρ	air density	C_s	regression-based sensitivity factor
W_g	amplitude of the gust	w_g	normal component of the gust velocity
ϕ_w	power spectral density function	L_g	gust scale
σ_w	ratio of gust scale to freestream velocity	τ_w	root-mean-square velocity of gust
r	root mean square	ω	circular frequency
η	gust alleviation rate	Ω	spatial circular frequency

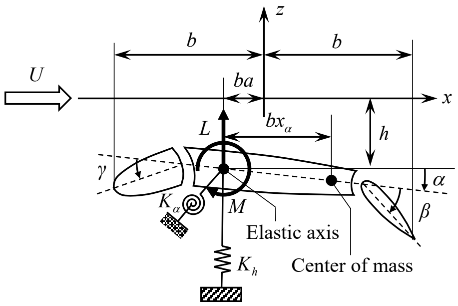

Fig. 1. 2-DOF wing model with control surfaces.

The dynamic equation of this system is as follows:

$$\begin{bmatrix} m_{\mathrm{T}} & m_{\mathrm{W}} x_\alpha b \\ m_{\mathrm{W}} x_\alpha b & I_\alpha \end{bmatrix} \begin{bmatrix} \ddot{h} \\ \ddot{\alpha} \end{bmatrix} + \begin{bmatrix} c_h & 0 \\ 0 & c_\alpha \end{bmatrix} \begin{bmatrix} \dot{h} \\ \dot{\alpha} \end{bmatrix} + \begin{bmatrix} k_h & 0 \\ 0 & k_\alpha(\alpha) \end{bmatrix} \begin{bmatrix} h \\ \alpha \end{bmatrix} = \begin{bmatrix} -L \\ M \end{bmatrix} \tag{1}$$

where $k_\alpha(\alpha)$ is the nonlinear pitch stiffness of this system [45], and has the following expression.

$$k_\alpha(\alpha) = 12.77 + 53.47\alpha + 1003\alpha^2 \tag{2}$$

In Eq. (1), the L and M are quasi-steady aerodynamic force and moment [45], including LE and TE control surfaces, which are defined as

$$\begin{cases} L = \rho U^2 bsC_{l\alpha}\left[\alpha + \left(\dot{h}/U\right) + \left(\frac{1}{2} - a\right) b(\dot{\alpha}/U)\right] \\ \quad +\rho U^2 bsC_{l\beta}\beta + \rho U^2 bsC_{l\gamma}\gamma \\ M = \rho U^2 b^2 sC_{m\alpha-\mathrm{eff}}\left[\alpha + \left(\dot{h}/U\right) + \left(\frac{1}{2} - a\right) b(\dot{\alpha}/U)\right] \\ \quad +\rho U^2 b^2 sC_{m\beta-\mathrm{eff}}\beta + \rho U^2 b^2 sC_{m\gamma-\mathrm{eff}}\gamma \end{cases} \tag{3}$$

where $C_{m\alpha-\mathrm{eff}}$, $C_{m\beta-\mathrm{eff}}$, and $C_{m\gamma-\mathrm{eff}}$ are the effective dynamic and control moment derivatives due to pitch angle and control surfaces deflection [45]. Parameters $C_{m\alpha-\mathrm{eff}}$, $C_{m\beta-\mathrm{eff}}$, and $C_{m\gamma-\mathrm{eff}}$, representing the effective moment coefficients about the elastic axis in the α, β and γ directions, are written as

$$\begin{cases} C_{m\alpha-\mathrm{eff}} = \left(\frac{1}{2} + a\right) C_{l\alpha} + 2C_{m\alpha} \\ C_{m\beta-\mathrm{eff}} = \left(\frac{1}{2} + a\right) C_{l\beta} + 2C_{m\beta} \\ C_{m\gamma-\mathrm{eff}} = \left(\frac{1}{2} + a\right) C_{l\gamma} + 2C_{m\gamma} \end{cases} \tag{4}$$

The system parameters are given in TABLE II.

TABLE II System parameters of 2-DOF wing section model [45]

Parameter	Value	Parameter	Value
b	0.1905 m	$C_{l\alpha}$	6.757
a	−0.6719	$C_{l\beta}$	3.774
x_α	0.5721	$C_{l\gamma}$	−0.1566
s	0.5945 m	$C_{m\alpha}$	0
m_{W}	5.230 kg	$C_{m\beta}$	−0.6719
m_{T}	15.57 kg	$C_{m\gamma}$	−0.1005
I_α	$0.1419\ \mathrm{kg\cdot m^2}$	ρ	$1.225\ \mathrm{kg/m^3}$
c_h	$27.43\ \mathrm{kg/s}$	k_h	$2844\ \mathrm{N/m}$
c_α	$0.0360\ \mathrm{kg\cdot m^2/s}$		

For this 2-DOF system, the state and output variables are defined as

$$\begin{cases} \boldsymbol{x} = [\dot{h} \quad \dot{\alpha} \quad h \quad \alpha]^T \\ \boldsymbol{y} = [h \quad \alpha]^T \end{cases} \tag{5}$$

Eq. (1) and (2) are combined to form the following state-space form

$$\begin{cases} \dot{\boldsymbol{x}} = \boldsymbol{A}(\boldsymbol{x})\boldsymbol{x} + \boldsymbol{B}\boldsymbol{u} \\ \boldsymbol{y} = \boldsymbol{C}\boldsymbol{x} \end{cases} \tag{6}$$

The matrices are shown as

$$\begin{cases} \boldsymbol{A} = \begin{bmatrix} -c_1 & -c_2 & -k_1 & -(k_2 + q_{\alpha 1}(\alpha)) \\ -c_3 & -c_4 & -k_3 & -(k_4 + q_{\alpha 2}(\alpha)) \\ 1 & 0 & 0 & 0 \\ 0 & 1 & 0 & 0 \end{bmatrix} \\ \boldsymbol{B} = \begin{bmatrix} d_1 & d_2 \\ d_3 & d_4 \\ 0 & 0 \\ 0 & 0 \end{bmatrix} \\ \boldsymbol{C} = \begin{bmatrix} 0 & 0 & 1 & 0 \\ 0 & 0 & 0 & 1 \end{bmatrix} \\ \boldsymbol{u} = \begin{bmatrix} \beta \\ \gamma \end{bmatrix} \end{cases} \tag{7}$$

where p_α and q_α are nonlinear parameters in the system. All the system parameters in (6) are defined as

$$\begin{cases} D = \begin{vmatrix} m_{\mathrm{T}} & \mathrm{m_W} x_\alpha b \\ \mathrm{m_W} x_\alpha b & I_\alpha \end{vmatrix} \\ k_1 = I_\alpha k_h / D \\ k_2 = (I_\alpha \rho U^2 b s C_{l\alpha} + m_{\mathrm{W}} x_\alpha \rho U^2 b^3 s C_{m\alpha-\mathrm{eff}})/D \\ k_3 = -m_{\mathrm{W}} x_\alpha b k_h / D \\ k_4 = (-m_{\mathrm{W}} x_\alpha \rho U^2 b^2 s C_{l\alpha} - m_{\mathrm{T}} \rho U^2 b^2 s C_{m\alpha-\mathrm{eff}})/D \\ c_1 = [I_\alpha (c_h + \rho U b s C_{l\alpha}) + m_{\mathrm{W}} x_\alpha \rho U b^3 s C_{m\alpha-\mathrm{eff}}]/D \\ c_2 = [I_\alpha \rho U b^2 s C_{l\alpha}(1/2 - a) - m_{\mathrm{W}} x_\alpha b c_\alpha + \\ \quad m_{\mathrm{W}} x_\alpha \rho U b^4 s C_{m\alpha-\mathrm{eff}}(1/2 - a)]/D \\ c_3 = [-m_{\mathrm{W}} x_\alpha b (c_h + \rho U b s C_{l\alpha}) - \\ \quad m_{\mathrm{T}} \rho U b^2 s C_{m\alpha-\mathrm{eff}}/D \\ c_4 = [-m_{\mathrm{W}} x_\alpha \rho U b^3 s C_{l\alpha}(1/2 - a) + m_{\mathrm{T}} c_\alpha - \\ \quad m_{\mathrm{T}} \rho U b^3 s C_{m\alpha-\mathrm{eff}}(1/2 - a)]/D \\ d_1 = \left(-I_\alpha \rho U^2 b s C_{l\beta} - m_{\mathrm{W}} x_\alpha \rho U^2 b^3 s C_{m\beta-\mathrm{eff}}\right)/D \\ d_2 = \left(-I_\alpha \rho U^2 b s C_{l\gamma} - m_{\mathrm{W}} x_\alpha \rho U^2 b^3 s C_{m\gamma-\mathrm{eff}}\right)/D \\ d_3 = \left(m_{\mathrm{W}} x_\alpha \rho U^2 b^2 s C_{l\beta} + m_{\mathrm{T}} \rho U^2 b^2 s C_{m\beta-\mathrm{eff}}\right)/D \\ d_4 = \left(m_{\mathrm{W}} x_\alpha \rho U^2 b^2 s C_{l\gamma} + m_{\mathrm{T}} \rho U^2 b^2 s C_{m\gamma-\mathrm{eff}}\right)/D \\ q_{\alpha 1}(\alpha) = -(m_{\mathrm{W}} x_\alpha b / D) k_\alpha(\alpha) \\ q_{\alpha 2}(\alpha) = (m_{\mathrm{T}}/D) k_\alpha(\alpha) \end{cases} \tag{8}$$

where parameter D is the determinant of the mass matrix of this 2-DOF wing system.

$$D = m_{\mathrm{T}} I_\alpha - (m_{\mathrm{W}} x_\alpha b)^2 = m_{\mathrm{T}}\left[I_{cg} + m_{\mathrm{W}} (x_\alpha b)^2\right] - (m_{\mathrm{W}} x_\alpha b)^2 > 0 \tag{9}$$

where parameter $I_{cg} > 0$ is the total mass moment of inertia about center of mass. From Eq. (9), the derivation shows that the determinant D is positive.

3 Inverse dynamic control scheme and stability judgement

3.1 Obtaining the reference trajectory

For the inverse dynamic method, a reference trajectory is necessary to design the control law. The desired path can be obtained through the following steps, as shown in Fig. 2. Assuming one smooth nonlinear time-invariant system $\mathcal{A}$ admits a Jacobian linearization, it may be reducible to a linear time-invariant (LTI) system $\mathcal{B}$. For system $\mathcal{B}$, it may be controlled by classic linear control methods, such as LQR approach [6]. This approach generates a globally smooth output trajectory $\boldsymbol{y}(t)$ from the initial state to the equilibrium, which is adopted as the reference trajectory $\boldsymbol{y}^*(t)$ for the inverse dynamic method.

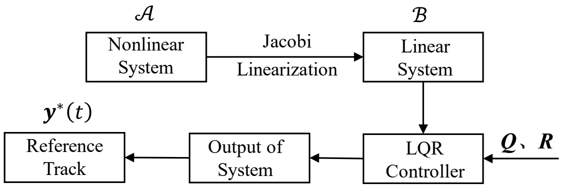

Fig. 2. Nonlinear system linearization to obtain the reference track.

Assuming system $\mathcal{A}$ can be transformed into a state-space representation analogous to that presented in Eq. (6), its controllability may be analyzed through the inverse dynamic method. System $\mathcal{A}$ may be written as

$$\mathcal{A}: \begin{cases} \dot{\boldsymbol{x}}(t) = f(\boldsymbol{x}(t)) + \boldsymbol{B}_1 \boldsymbol{u}(t) \\ \boldsymbol{y}(t) = \boldsymbol{C}_1 \boldsymbol{x}(t) \end{cases} \quad t \in [0, T] \tag{10}$$

where $\boldsymbol{x}(t) = [x_1\ x_2\ \cdots\ x_m]^{\mathrm{T}} \in \mathbb{R}^m$ is the vector of system state, $\boldsymbol{y}(t) = [y_1\ y_2\ \cdots\ y_l]^{\mathrm{T}} \in \mathbb{R}^l$ is the vector of outputs, $\boldsymbol{u}(t) = [u_1\ u_2\ \cdots\ u_n]^{\mathrm{T}} \in \mathbb{R}^n$ is the vector of inputs, $f(\cdot)$ is a smooth nonlinear function of dynamic process, $\boldsymbol{B}_1 \in \mathbb{R}^{m\times n}$ and $\boldsymbol{C}_1 \in \mathbb{R}^{l\times m}$ are constant matrices. The generic boundary conditions and constraints of this system are defined as follows:

$$\begin{cases} \boldsymbol{x}(0) = \boldsymbol{x}_0 \\ \boldsymbol{x}(T) = \boldsymbol{x}_T \end{cases} \tag{11}$$

Due to the higher difficulty of controlling a nonlinear system than a linear system, the nonlinear system $\mathcal{A}$ may be linearized first to get linear system $\mathcal{B}$. A commonly-used method to obtain a linear system is the Jacobian linearization [46]. To clearly demonstrate the linearization process, one case of the nonlinear time-invariant system is chosen as follows:

$$
\dot{\boldsymbol{x}}(t) = f(\boldsymbol{x}(t)) \rightarrow \begin{cases} \dot{x}_1 = f_1(x_1\, x_2\, \cdots\, x_m) \\ \dot{x}_2 = f_2(x_1\, x_2\, \cdots\, x_m) \\ \cdots \\ \dot{x}_m = f_m(x_1\, x_2\, \cdots\, x_m) \end{cases} \tag{12}
$$

where the vector of inputs $\boldsymbol{u}(t)$ is not considered. The equilibrium point of this system is assumed as $\dot{\boldsymbol{x}}|_{\boldsymbol{x}=\boldsymbol{x}^*} = f(\boldsymbol{x}^*) = \boldsymbol{0}$. Assuming the function f admits a computable derivative at the equilibrium point, the truncated Taylor expansion at the equilibrium point is written as

$$
\begin{aligned} \dot{\boldsymbol{x}} &\approx f(\boldsymbol{x}^*) + \begin{bmatrix} \frac{\partial f_1}{\partial x_1} & \cdots & \frac{\partial f_1}{\partial x_m} \\ \vdots & \ddots & \vdots \\ \frac{\partial f_m}{x_1} & \cdots & \frac{\partial f_m}{\partial x_m} \end{bmatrix} (\boldsymbol{x} - \boldsymbol{x}^*) \\ &= \boldsymbol{0} + \boldsymbol{A}_1(\boldsymbol{x} - \boldsymbol{x}^*) \end{aligned} \tag{13}
$$

where $\boldsymbol{A}_1 \in \mathbb{R}^{m\times m}$ is a constant matrix. If the equilibrium point is the origin, this equation may be simplified as $f(\boldsymbol{x}) \approx \boldsymbol{A}_1\boldsymbol{x}$. Thus, the nonlinear time-invariant system $\mathcal{A}$ may be linearized to a linear system $\mathcal{B}$, which can be written as

$$
\mathcal{B}\colon \begin{cases} \dot{\boldsymbol{x}}(t) = \boldsymbol{A}_1\boldsymbol{x}(t) + \boldsymbol{B}_1\boldsymbol{u}(t) \\ \boldsymbol{y}(t) = \boldsymbol{C}_1\boldsymbol{x}(t) \end{cases} \tag{14}
$$

The system $\mathcal{B}$ is a general form of a smooth LTI system. According to LQR approach, the cost function is defined as

$$
J = \int_0^{\tau} (\boldsymbol{x}^{\mathrm{T}}\boldsymbol{Q}\boldsymbol{x} + \boldsymbol{u}^{\mathrm{T}}\boldsymbol{R}\boldsymbol{u})dt \tag{15}
$$

where $\boldsymbol{Q} \in \mathbb{R}^{m\times m}$ and $\boldsymbol{R} \in \mathbb{R}^{n\times n}$ are constant diagonal semi-positive definite matrices, and have the following forms.

$$
\begin{cases} \boldsymbol{Q} = Diag\{q_1, q_2, \cdots, q_m\} & (q_i \geq 0;\ i = 1,2\cdots, m) \\ \boldsymbol{R} = Diag\{r_1, r_2, \cdots, r_n\} & \left(r_j \geq 0;\ j = 1,2\cdots, n\right) \end{cases} \tag{16}
$$

The choice of feedback gain matrices depends on the specific problem. For example, when controlling the plunge direction presents a greater degree of difficulty, a larger weighting coefficient q_i is typically assigned. The outputs of system $\mathcal{B}$ can be written as

$$
\boldsymbol{y}(t) = \boldsymbol{C}_1 e^{(\boldsymbol{A}_1 - \boldsymbol{B}_1\boldsymbol{K}_1)t}\boldsymbol{x}_0 \tag{17}
$$

where $\boldsymbol{K}_1$ is the gain matrix, which is obtained by solving the Riccati equation [6].

This output trajectory can be used as a reference track $\boldsymbol{y}^*(t)$ in the inverse dynamic control process. Replacing the system $\mathcal{A}$ with the 2-DOF wing system in (6), the desired path to suppress flutter can be solved directly.

3.2 Inverse dynamic method

The concept of the inverse dynamic method is the equivalent transformation from the nonlinear dynamic system to a decoupled linear system [40]. For nonlinear system $\mathcal{A}$, the process of the control law design using the inverse dynamic method is shown in Fig. 3. The idea of the inverse dynamic method is to explore a control vector $\boldsymbol{u}(t)$ to track a desired output trajectory $\boldsymbol{y}^*(t)$ by satisfying the boundary condition, and can be expressed as

$$\lim_{t\to\infty} \boldsymbol{e}(\boldsymbol{y}(t), \boldsymbol{y}^*(t), t) = \lim_{t\to\infty} [\boldsymbol{y}(t) - \boldsymbol{y}^*(t)] = \boldsymbol{0} \tag{18}$$

where $\boldsymbol{e}(\cdot)$ is a continuous constraint function, representing the tracking error of the system $\mathcal{A}$. By defining one feedback term, the control problem of nonlinear systems can be transformed into the convergence problem of the error system. Then, the inverse dynamic method is extended to obtain the control law.

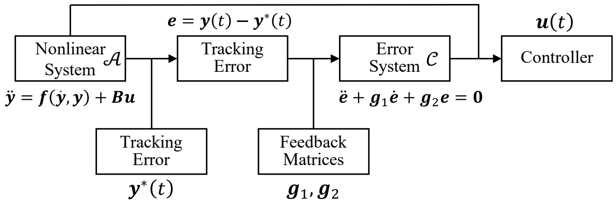

Fig. 3. Control law design through the inverse dynamic method.

Regarding the dynamic equations in Eq. (1), it can be equivalently reformulated as

$$\begin{bmatrix} m_\mathrm{T} & \mathrm{m}_\mathrm{W} x_\alpha b \\ m_\mathrm{W} x_\alpha b & I_\alpha \end{bmatrix} \ddot{\boldsymbol{y}} = \boldsymbol{f}(\boldsymbol{y}, \dot{\boldsymbol{y}}) + \begin{bmatrix} d_1 & d_2 \\ d_3 & d_4 \end{bmatrix} \boldsymbol{u} \tag{19}$$

In Eq. (19), since the output variable $\boldsymbol{y}(t)$ inherently involves second-order forms, the constraint vector $\boldsymbol{e}$ must be differentiated twice to establish an explicit dependence on $\ddot{\boldsymbol{y}}$ in the system description. Consequently, the vector of inputs $\boldsymbol{u}(t)$ can be associated with the constraint function $\boldsymbol{e}$, and the relationship is formally expressed as

$$\begin{bmatrix} m_\mathrm{T} & \mathrm{m}_\mathrm{W} x_\alpha b \\ m_\mathrm{W} x_\alpha b & I_\alpha \end{bmatrix} (\ddot{\boldsymbol{e}} + \ddot{\boldsymbol{y}}^*) = \boldsymbol{f}(\boldsymbol{y}, \dot{\boldsymbol{y}}) + \begin{bmatrix} d_1 & d_2 \\ d_3 & d_4 \end{bmatrix} \boldsymbol{u} \tag{20}$$

The input vector $\boldsymbol{u}$ can be determined from Eq. (20) once other variables are specified. In addition, a feedback term may be added instead of defining the second order derivative of constraint vector $\ddot{\boldsymbol{e}}$ to be null. The feedback item consisting of constraint vector $\boldsymbol{e}$ and its differential $\dot{\boldsymbol{e}}$ is defined as

$$\ddot{\boldsymbol{e}} = -\boldsymbol{g}_1\dot{\boldsymbol{e}} - \boldsymbol{g}_2\boldsymbol{e} \tag{21}$$

where $\boldsymbol{g}_1$and $\boldsymbol{g}_2$ are diagonal constant gain matrices, with their selection critically determining the convergence rate of the error dynamics, and can be written as

$$\begin{cases} \boldsymbol{g}_1 = Diag\{g_{11}, g_{12}, \cdots, g_{1l}\} \\ \boldsymbol{g}_2 = Diag\{g_{21}, g_{22}, \cdots, g_{2l}\} \\ \quad (g_{1i}, g_{2i} > 0;\ i = 1,2 \cdots, l) \end{cases} \tag{22}$$

Under the proposed control law, the nonlinear system $\mathcal{A}$ is transformed into the error system $\mathcal{C}$, as shown in Fig. 3, and can be written as

$$\mathcal{C}: \ddot{\boldsymbol{e}} + \boldsymbol{g}_1\dot{\boldsymbol{e}} + \boldsymbol{g}_2\boldsymbol{e} = \boldsymbol{0} \tag{23}$$

The convergence rate of the closed-loop system is directly determined by the designed error system $\mathcal{C}$, through the gain matrices $\boldsymbol{g}_1$ and $\boldsymbol{g}_2$. At the same time, the system $\mathcal{C}$ has the same form as the linear spring vibration system, whose form can be expressed by

$$\ddot{x} + k\dot{e} + ce = 0 \tag{24}$$

where k and c are the stiffness and damping coefficients, respectively.

The comparison between these two systems is shown in Fig. 4. Fig. 4 (a) illustrates the error system $\mathcal{C}$ of a nonlinear 2-DOF wing system and Fig. 4 (b) shows one classical linear spring system. It is clear that the error system $\mathcal{C}$ may be equivalent to multiple independent linear spring systems. The gain matrices $\boldsymbol{g}_1$ and $\boldsymbol{g}_2$ represent the stiffness and damping of the system $\mathcal{C}$. That is to say, the error system $\mathcal{C}$ also converges exponentially. In the system $\mathcal{C}$, the stiffness matrix $\boldsymbol{g}_2$ stands for the natural frequency of the undamped vibration. The speed of convergence mainly depends on the damping matrix $\boldsymbol{g}_1$. In the 2-DOF wing flutter problem, the time domain response of two directions needs to converge to a constant quickly. Therefore, the over damping condition is the best choice for this problem, and is defined as follows:

$$\xi_{ei} = \frac{g_{1i}}{2\sqrt{g_{2i}}} > 1;\ i = 1,2 \cdots, l \tag{25}$$

where ξ_{ei} is the damping ratio of the error system, g_{1i} and g_{2i} are i^{th} elements in the gain matrices $\boldsymbol{g}_1$ and $\boldsymbol{g}_2$. In this condition, system state variables may quickly converge to the desired path. In addition, (23) may be combined with (10) and (18) to obtain the desired inputs $\boldsymbol{u}(t)$ for this nonlinear system $\mathcal{A}$.

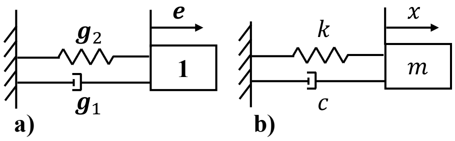

Fig. 4. Comparison of the two systems, (a) error system; (b) linear spring system.

Similarly, the system $\mathcal{A}$ may be replaced with the 2-DOF wing system in (6). Before that, the 2-DOF wing system state space may be rewritten as

$$\begin{cases} \dot{\boldsymbol{x}} = \begin{bmatrix} \boldsymbol{A}_{11} & \boldsymbol{A}_{12}(\alpha) \\ \boldsymbol{E}_1 & \boldsymbol{O}_1 \end{bmatrix} \boldsymbol{x} + \begin{bmatrix} \boldsymbol{B}_{11} \\ \boldsymbol{O}_1 \end{bmatrix} \boldsymbol{u} \\ \boldsymbol{y} = [\boldsymbol{O}_1 \quad \boldsymbol{E}_1] \boldsymbol{x} \end{cases} \tag{26}$$

where $\boldsymbol{x}$ and $\boldsymbol{y}$ have been defined in (5), $\boldsymbol{E}_1 \in \mathbb{R}^{2\times2}$ is the identity matrix, $\boldsymbol{O}_1 \in \mathbb{R}^{2\times2}$ is the zero matrix, $\boldsymbol{A}_{11}$, $\boldsymbol{A}_{12}$ and $\boldsymbol{B}_{11}$ are respectively a part of the system matrices $\boldsymbol{A}$ and $\boldsymbol{B}$ in (7), and are defined as

$$\begin{cases} \boldsymbol{A}_{11} = \begin{bmatrix} -c_1 & -c_2 \\ -c_3 & -c_4 \end{bmatrix} \\ \boldsymbol{A}_{12}(\alpha) = \begin{bmatrix} -k_1 & -(k_2 + q_{\alpha1}(\alpha)) \\ -k_3 & -(k_4 + q_{\alpha2}(\alpha)) \end{bmatrix} \\ \boldsymbol{B}_{11} = \begin{bmatrix} d_1 & d_2 \\ d_3 & d_4 \end{bmatrix} \end{cases} \tag{27}$$

Consider the matrix $\boldsymbol{B}_{11}$, its determinant is given by:

$$\begin{aligned} \det(\boldsymbol{B}_{11}) &= \begin{vmatrix} d_1 & d_2 \\ d_3 & d_4 \end{vmatrix} \\ &= 2\rho^2 U^4 b^3 s^2 (C_{l\gamma} C_{m\beta} - C_{l\beta} C_{m\gamma})/D \end{aligned} \tag{28}$$

where parameter $D(\neq 0)$ has been defined in (8). The signs of the aerodynamic force and moment coefficients are related by:

$$\begin{cases} \operatorname{sign}(C_{l\gamma}) = \operatorname{sign}(C_{m\gamma}) \\ \operatorname{sign}(C_{l\beta}) = -\operatorname{sign}(C_{m\beta}) \end{cases} \tag{29}$$

Since the condition $C_{l\gamma} C_{m\beta} - C_{l\beta} C_{m\gamma} = 0$ is improbable under the sign relationships in Eq. (29), the determinant of $\boldsymbol{B}_{11}$ is non-zero. Therefore, the matrix $\boldsymbol{B}_{11}$ is invertible, and the inverse dynamics control law in Eq. (32) is well-defined.

Since the desired path $\boldsymbol{y}^*(t)$ has been obtained in (17), it may be combined with the feedback item.

$$\ddot{\boldsymbol{y}} = \ddot{\boldsymbol{y}}^* - \boldsymbol{g}_1(\dot{\boldsymbol{y}} - \dot{\boldsymbol{y}}^*) - \boldsymbol{g}_2(\boldsymbol{y} - \boldsymbol{y}^*) \tag{30}$$

where $\boldsymbol{g}_1 \in \mathbb{R}^{2\times 2}$ and $\boldsymbol{g}_2 \in \mathbb{R}^{2\times 2}$ are constant diagonal positive definite matrices. Substituting (30) into (26), only the first two sets of equations are retained, viz

$$\ddot{\boldsymbol{y}}^* = \boldsymbol{A}_{11}\dot{\boldsymbol{y}} + \boldsymbol{A}_{12}\boldsymbol{y} + \boldsymbol{B}_{11}\boldsymbol{u} + \boldsymbol{g}_1(\dot{\boldsymbol{y}} - \dot{\boldsymbol{y}}^*) + \boldsymbol{g}_2(\boldsymbol{y} - \boldsymbol{y}^*) \tag{31}$$

Thus, the desired control vector $\boldsymbol{u}$ is solved as

$$\boldsymbol{u} = \boldsymbol{B}_{11}^{-1}[(\ddot{\boldsymbol{y}}^* + \boldsymbol{g}_1\dot{\boldsymbol{y}}^* + \boldsymbol{g}_2\boldsymbol{y}^*) - (\boldsymbol{g}_1 + \boldsymbol{A}_{11})\dot{\boldsymbol{y}} - (\boldsymbol{g}_2 + \boldsymbol{A}_{12})\boldsymbol{y}] \tag{32}$$

3.3 Closed-loop stability

Before proceeding with the stability analysis, the following assumptions are stated.

Assumption 1: The control effectiveness matrix $\boldsymbol{B}_{11}$ is invertible, as justified by the determinant analysis from Eq. (27) to Eq. (29).

Assumption 2: The aerodynamic terms in $\boldsymbol{A}_{11}$ and the nonlinear stiffness functions $q_{\alpha 1}(\alpha)$ and $q_{\alpha 2}(\alpha)$ in $\boldsymbol{A}_{12}(\alpha)$ are smooth and bounded for all states within the considered flight envelope.

Assumption 3**:** The actuator does not saturate during nominal operation. The control input computed from Eq. (32) is assumed to remain within the physical limits.

The 2-DOF wing system is a smooth nonlinear time-invariant system, satisfying the applicable conditions of the second method of Lyapunov. In order to check stability of the closed-loop system in (6), the Lyapunov candidate function is defined as

$$V(\boldsymbol{x}) = \frac{1}{2}(\boldsymbol{x} - \boldsymbol{x}^*)^T \begin{bmatrix} \boldsymbol{E}_1 & \boldsymbol{0} \\ \boldsymbol{0} & \boldsymbol{g}_2 \end{bmatrix} (\boldsymbol{x} - \boldsymbol{x}^*) \tag{33}$$

where $\boldsymbol{x}^* = [\dot{\boldsymbol{y}}^* \ \boldsymbol{y}^*]^{\mathrm{T}}$ is the desired path of state variables, $\boldsymbol{E}_1 \in \mathbb{R}^{2\times 2}$ is the identity matrix, $\boldsymbol{g}_1$and $\boldsymbol{g}_2$ are same in (30), $V(\cdot): \mathbb{R}^4 \to \mathbb{R}$ is a smooth Lyapunov candidate function. Given the positive definite diagonal matrices $\boldsymbol{E}_1$ and $\boldsymbol{g}_2$, the quadratic form $V(\boldsymbol{x})$ satisfies $V(\boldsymbol{x}) \geq 0$ for all $\boldsymbol{x}$, and $V(\boldsymbol{x}) = 0$ only if $\boldsymbol{x} = \boldsymbol{x}^*$. The time derivative of the Lyapunov candidate function is as follows:

$$\dot{V}(\boldsymbol{x}) = (\dot{\boldsymbol{x}} - \dot{\boldsymbol{x}}^*)^T \begin{bmatrix} \boldsymbol{E}_1 & \boldsymbol{0} \\ \boldsymbol{0} & \boldsymbol{g}_2 \end{bmatrix} (\boldsymbol{x} - \boldsymbol{x}^*) \tag{34}$$

To determine the sign of $\dot{V}(\boldsymbol{x})$, the control law (32) is first substituted into the system dynamics (26). This substitution cancels the nonlinear stiffness terms $q_{\alpha 1}(\alpha)$ and $q_{\alpha 2}(\alpha)$ in $\boldsymbol{A}_{12}(\alpha)$ and the quasi-steady aerodynamic terms in $\boldsymbol{A}_{11}$. After simplification, the closed-loop error dynamics is as follows:

$$(\ddot{\boldsymbol{y}}-\ddot{\boldsymbol{y}}^*)+\boldsymbol{g}_1(\dot{\boldsymbol{y}}-\dot{\boldsymbol{y}}^*)+\boldsymbol{g}_2(\boldsymbol{y}-\boldsymbol{y}^*)=\boldsymbol{0} \tag{35}$$

Substituting the error dynamics (35) into the Lyapunov derivative (34) gives

$$\begin{aligned}\dot{V}(\boldsymbol{x}) &= (\boldsymbol{x}-\boldsymbol{x}^*)^T\begin{bmatrix}-\boldsymbol{g}_1 & \boldsymbol{0}\\ \boldsymbol{0} & \boldsymbol{0}\end{bmatrix}(\boldsymbol{x}-\boldsymbol{x}^*)\\ &= -(\dot{\boldsymbol{y}}-\dot{\boldsymbol{y}}^*)^T\boldsymbol{g}_1(\dot{\boldsymbol{y}}-\dot{\boldsymbol{y}}^*)\end{aligned} \tag{36}$$

From Eq. (36), $\dot{V}(\boldsymbol{x})\leq 0$ for all $\boldsymbol{x}$. Since $V(\boldsymbol{x})$ is positive definite and $\dot{V}(\boldsymbol{x})$ is negative semi-definite, the closed-loop system is stable with respect to the reference trajectory $\boldsymbol{x}^*(t)$ by the second method of Lyapunov. To establish asymptotic convergence, LaSalle's invariance principle is invoked. Let $\Omega=\{x|V(x)\leq V(x_0)\}$ be a level set containing the initial state. Because $\dot{V}(x)\leq 0$, Ω is positively invariant. By LaSalle's principle, every trajectory starting in Ω approaches the largest invariant set Γ contained in the set where $\dot{V}(\boldsymbol{x})=0$.

From Eq. (36), $\dot{V}(\boldsymbol{x})=0$ requires $\dot{\boldsymbol{y}}=\dot{\boldsymbol{y}}^*$. Since $\dot{\boldsymbol{y}}\equiv\dot{\boldsymbol{y}}^*$ on the invariant set, their time derivatives also coincide, which means $\ddot{\boldsymbol{y}}\equiv\ddot{\boldsymbol{y}}^*$. Substituting these two conditions into the linear error dynamics (35), it gives

$$\boldsymbol{g}_2(\boldsymbol{y}-\boldsymbol{y}^*)=\boldsymbol{0} \tag{37}$$

Since $\boldsymbol{g}_2$ is positive definite, it follows that $\boldsymbol{y}=\boldsymbol{y}^*$. Therefore, the largest invariant set is $\Gamma=\{x^*\}$, i.e., the desired equilibrium point. By LaSalle's principle, the tracking error converges asymptotically to zero. The reference trajectory $\boldsymbol{y}^*$ is designed via LQR method to converge to the equilibrium at the terminal time. Combining the convergence of the tracking error with that of the reference trajectory, the system states satisfy

$$\begin{cases}\lim\limits_{t\to\infty}\boldsymbol{y}(t)=\lim\limits_{t\to\infty}\boldsymbol{y}^*(t)=\boldsymbol{0}\\ \lim\limits_{t\to\infty}\dot{\boldsymbol{y}}(t)=\lim\limits_{t\to\infty}\dot{\boldsymbol{y}}^*(t)=\boldsymbol{0}\end{cases} \tag{38}$$

Therefore, the flutter of the 2-DOF wing system can be suppressed by the proposed inverse dynamic method with a reference trajectory. The above stability analysis assumes that the actuator does not saturate. If the required control input exceeds the actuator limits, the exact cancellation in Eq. (32) no longer holds, and the tracking performance may degrade. It is also noted that the present study adopts a quasi-steady aerodynamic model, which neglects unsteady effects, compressibility, and dynamic stall. Under an unsteady formulation, the nominal cancellation would not be exact, which may similarly affect the controllability of the system. A full investigation under unsteady aerodynamics is beyond the present scope and is included in the future work directions. A simulation study is presented in the next section to evaluate the control performance under practical conditions.

4 Simulations and results

4.1 Linearized system simulation

For this problem, it is clear that the control scheme requires a reference trajectory. In this paper, the nonlinear part of this 2-DOF wing system is the pitch stiffness k_α in (2). The nonlinear system in (6) may be linearized as presented for system $\mathcal{A}$ in (12). The linear part of the initial system remains unchanged and the new pitch stiffness of the linear system is written as

$$\tilde{k}_\alpha = 12.77\ \mathrm{N \cdot m} \tag{39}$$

For this linearized system, the LQR method is used to obtain the output curves of the state variables. The boundary condition of the reference trajectory is defined as $\boldsymbol{x}(\boldsymbol{0}) = \boldsymbol{x}_0$ and $\boldsymbol{x}(T) = \boldsymbol{0}$. The gain matrices $\boldsymbol{Q}$ and $\boldsymbol{R}$ are assumed as

$$\begin{cases} \boldsymbol{Q} = Diag\{q_1, q_2, q_3, q_4\} \\ \boldsymbol{R} = r_1 \end{cases} \tag{40}$$

Considering the convergence rate of this model as well as the difficulty of controlling the plunge direction in the system, the relation of the parameters is defined as follows

$$q_1 = q_3 = 10 > r_1 = 5 > q_2 = q_4 = 1 \tag{41}$$

The flow velocity is selected as $U = 12\ \mathrm{m/s}$. This freestream velocity will lead to flutter of the original open-loop nonlinear system, and the result is shown in Fig. 5 (a) and (b). The initial conditions are defined with one positional disturbance and are chosen as

$$\boldsymbol{x}_0 = [0\ \mathrm{m/s} \quad 0\ \mathrm{rad/s} \quad 0.01\ \mathrm{m} \quad 0.1\ \mathrm{rad}]^{\mathrm{T}} \tag{42}$$

The fourth order Runge-Kutta method is used to solve the equation of the linearized system by MATLAB. The desired output trajectory $\boldsymbol{y}^*(t)$ is shown in Fig. 5. This response result may be taken as the reference trajectory.

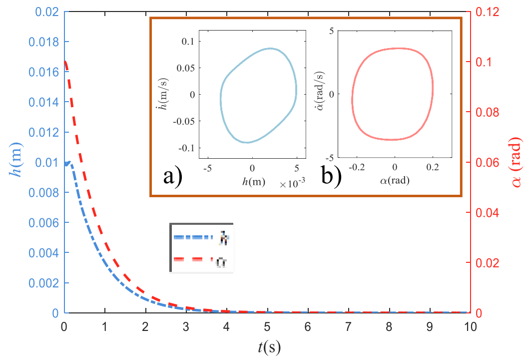

Fig. 5. The desired output trajectory of the nonlinear system at $U = 12$ m/s; and the phase diagrams (in the brown box) of the open-loop system simulations at $U = 12$ m/s, (a) $h - \dot{h}$ and (b) $\alpha - \dot{\alpha}$.

4.2 Nonlinear system simulation

In this section, the same initial conditions as in (42) are used in simulations. From simulations, the limit cycle oscillation (LCO) first appears at $U_0 = 9.8\ \mathrm{m/s}$. In wind-tunnel experiments [45], the LCO first occurs at $\sim 13\ \mathrm{m/s}$. Fig. 6 shows the phase diagrams of the open-loop system responses and the wind-tunnel experiments when flow velocity U is $13.01\ \mathrm{m/s}$. From Fig. 6, a discernible discrepancy between the two responses may be attributed to multiple contributing factors, including but not limited to modeling uncertainties, Coulomb friction effects, and the limitations of quasi-steady aerodynamic theory. Notably, the quasi-steady aerodynamic formulation yields a conservative estimate of the flutter onset speed. If controllability can be demonstrated under this more demanding condition, the control strategy is likely to remain effective in the actual system, where flutter onset occurs at a higher speed.

For the initial 2-DOF nonlinear wing system, the reference trajectory in Fig. 5 is combined with the inverse dynamic method to suppress flutter. To ensure that the error system is overdamped, the selection of $\boldsymbol{g}_1$ and $\boldsymbol{g}_2$ is constrained by the condition in (25). In addition, the selection of parameters $\boldsymbol{g}_1$ and $\boldsymbol{g}_2$ is not arbitrary due to the significant impact on system performance. One feasible set of gain matrices is chosen as

$$\begin{cases} \boldsymbol{g}_1 = Diag\{15, 25\} \\ \boldsymbol{g}_2 = Diag\{5, 5\} \end{cases} \tag{43}$$

In this case, the damping ratio $\xi_{e1,2}$ of the error system is much greater than 1. The initial conditions keep unchanged and the freestream velocity is set as $U = 12\ \mathrm{m/s}$, greater than the system LCO staring speed $U_0 = 9.8\ \mathrm{m/s}$.

In practical engineering contexts, the control surfaces are fundamentally limited by physical saturation constraints. Let $\boldsymbol{u}_s = S(\boldsymbol{u})$ be the saturated input, where $S(\cdot)$ is the saturation function defined below.

$$S(u) = \begin{cases} u_{\max}, & u > u_{\max} \\ u, & |u| \le u_{\max} \\ -u_{\max}, & u < -u_{\max} \end{cases} \tag{44}$$

where $u_{\max}$ denotes the maximum permissible deflection angle of the control surface.

In this case, a saturation limit of $u_{\max} = 20$ deg is imposed on the control surface deflections [47]. The reference trajectory is defined over the time interval [0,10] s with a constant time step of $T_s = 0.01$ s. In this situation, the inverse dynamic method is evaluated through simulations to suppress the

LCOs, as shown in Fig. 7. Obviously, all the state variables converge to zero after a transitory vibration within approximately $5 - 6$ s with the deflection limitation of the control surface. To provide a more intuitive measure of the control performance, the settling time T_{settle} is defined as the time required for all system output signals to settle within 1 % of their initial perturbation values [48]. Based on this definition, the T_{settle} for the case shown in Fig. 7 is calculated to be 3.58 s. To validate the performance of the proposed approach, its results were evaluated alongside those of the control strategy reported in [49], which also addresses flutter suppression of a 2-DOF wing system. For a fair comparison, the same initial conditions and freestream velocity as in Fig. 7 were adopted. The control law from [49], was implemented on the present wing model using the original gains from that study ($g_1^{\mathrm{ref}} = 100, g_2^{\mathrm{ref}} = 10^6$). The resulting closed-loop responses of the plunge displacement, pitch angle, and control surface deflections are presented in Fig. 8 (a)-(c), respectively. The proposed control strategy therefore provides a considerably faster transient response, with a settling time of 3.58 s versus 9.46 s for the method in [49].

To quantitatively compare the control effort, the Integral of Squared Control Input (ISCI) is adopted. For the two control surfaces, the ISCI is defined as

$$J_{\mathrm{ISCI}} = \int_0^{T^{\mathrm{ref}}} [\beta^2(t) + \gamma(t)^2] \mathrm{d}t \tag{45}$$

$T^{\mathrm{ref}} = 20$ s is the total simulation time shown in Fig. 8. The ISCI represents the accumulated control energy and corresponds to the control-weighted term in the standard quadratic cost function. Under the same saturation limit of 20 deg and without rate restrictions, the proposed method yields an ISCI of $0.1415\ \mathrm{rad}^2 \cdot \mathrm{s}$, compared with $1.0733\ \mathrm{rad}^2 \cdot \mathrm{s}$ for the benchmark in [49]. This indicates that flutter suppression is achieved with lower overall actuator effort.

It should be noted that the feedback gain matrices are not uniquely determined. To examine the effect of different gain selections, three additional sets of simulations were performed with various combinations of $\boldsymbol{g}_1$ and $\boldsymbol{g}_2$, as presented in Fig. 9. Subfigures (a)-(c) correspond to $\boldsymbol{g}_1 = Diag\{5, 5\}$ and $\boldsymbol{g}_2 = Diag\{5, 5\}$; subfigures (d)-(f) correspond to $\boldsymbol{g}_1 = Diag\{5, 5\}$ and $\boldsymbol{g}_2 = Diag\{15, 25\}$; and subfigures (g)-(i) correspond to $\boldsymbol{g}_1 = Diag\{15,25\}$ and $\boldsymbol{g}_2 = Diag\{5, 5\}$. As shown in Fig. 9, it can be seen that raising $\boldsymbol{g}_1$ provides a greater improvement in flutter suppression performance than raising $\boldsymbol{g}_2$. This is reflected by both a smaller tracking error and a reduced tendency toward control surface saturation.

To further assess the numerical performance of the proposed method, the influence of T_s on both the control accuracy and the computational cost is examined. The simulation is repeated with several different time steps, namely 0.002 s, 0.005 s, 0.02 s, and 0.05 s. For each T_s, 50 independent closed-loop simulations were conducted. Both the settling time T_{settle} and the mean computation time per run T_{per} were recorded. The results are summarized in TABLE III. As the time step increases from 0.002 s to 0.05 s, the mean computation time per run decreases substantially, from 1.4065 s to 0.0964 s. In contrast, the settling time remains nearly unchanged across this range, varying by less than 1 %. The effect of the time step on the mean computation time per run and the settling time is illustrated in Fig. 10 (a) and Fig. 10 (b), respectively. This insensitivity of the settling time confirms that the numerical solution is already well converged with respect to the time step. Therefore, it is effective to suppress the flutter of a nonlinear aeroelastic system using the inverse dynamic method.

Evidently, relying solely on a single initial state point alone is insufficient. The admissible control domain of the system is further investigated under control surface saturation and rate constraints. The admissible control domain of this nonlinear system is computed subject to the following constraints:

$$\begin{cases} |\delta_c| \le u_{\max} = 20 \text{ deg} \\ |\dot{\delta}_c| \le 10, 20, 30, 40, 80 \text{ deg/s} \end{cases} \tag{46}$$

where $|\delta_c|$ and $|\dot{\delta}_c|$ denote deflection angle and maximum deflection rate, respectively.

The simulation results characterizing the admissible control domain are illustrated in the Fig. 11 below. Fig. 11 illustrates the admissible control domain of the nonlinear system under constraints of $|\delta_c| \le 20$ deg and varying maximum deflection rates. In Fig. 11, the initial condition in Eq. (42) is annotated with a four-pointed star marker in the figure. The admissible control domain of this nonlinear system progressively expands with increasing deflection rate $|\dot{\delta}_c|$. When the deflection rate limit of the control surface is increased from 10 to 40 deg/s, the marked point becomes fully controllable within the admissible domain. Therefore, under the initial condition in Eq. (42), the maximum allowable deflection rate must be at least 40 deg/s to guarantee system controllability.

In the LQR cost function, the relative weighting between the state weighting matrix $\boldsymbol{Q}$ and the control weighting matrix $\boldsymbol{R}$ determines the trade-off between the state convergence rate and the required control effort. The gain matrices are chosen as $\boldsymbol{g}_1 = Diag\{15,25\}$ and $\boldsymbol{g}_2 = Diag\{5, 5\}$. In this problem, the LQR weighting parameter r_1 is systematically adjusted to generate a set of distinct reference trajectories. The flutter suppression performance is subsequently evaluated under the initial condition in Eq. (42), subject to a maximum control surface deflection of 15 deg and a maximum deflection rate of 100 deg/s. Fig. 12 presents the closed-loop responses for 3 different reference trajectories under the initial condition in Eq. (42) for the flow velocity $U = 12$ m/s. Fig. 12 (a), (b) and (c) illustrate the simulation results obtained by adopting the identically zero trajectory. For subfigures (d)-(f) and (g)-(i), the reference trajectory is generated via LQR with $r_1 = 5$ and $r_1 = 76$, respectively. The three selected reference trajectories are listed in TABLE IV. The settling times T_{settle} for the three cases are given by

$$\begin{cases} T_{\text{settle1}} = 3.88\ \text{s} \\ T_{\text{settle2}} = 4.21\ \text{s} \\ T_{\text{settle3}} = 1.08\ \text{s} \end{cases} \tag{47}$$

As shown in Fig. 12, the reference trajectory has a significant influence on the settling time of flutter suppression. The parameter r_1 is then varied over a wider range to investigate its effect on the flutter suppression settling time. Fig. 13 shows the variation of the settling time with respect to r_1, where a clear nonlinear relationship is observed. With the settling time adopted as the selection criterion, favorable performance is achieved for values of r_1 in the range of 20 to 200. Within this interval, the settling times are consistently shorter than that obtained with the zero trajectory.

TABLE III Average computation time per run and settling time under different time steps.

T_s(s)	T_{per}(s)	T_{settle}(s)
0.002	1.4065	3.5840
0.005	0.3758	3.5800
0.01	0.1992	3.5800
0.02	0.1322	3.5600
0.05	0.0964	3.5500

TABLE IV Design of different reference trajectories

Case	**Trajectory**	***Q***	***R***
1	Zero trajectory	/	/
2	Trajectory from LQR	$Diag\{10,1,10,1\}$	5
3	Trajectory from LQR	$Diag\{10,1,10,1\}$	76

Although the control surface deflection rate $\dot{\delta}_c$ may affect the controllability region boundaries, in the subsequent simulations, this study prioritizes the impact of control surface saturation constraints $|\delta_c|$.

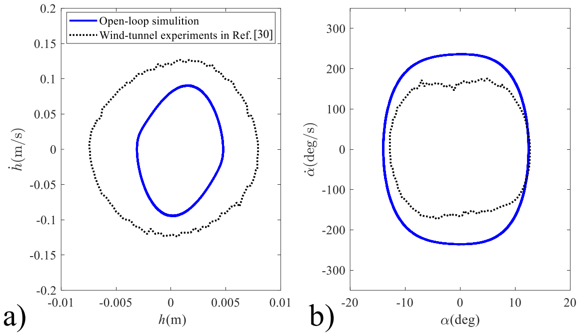

Fig. 6. Phase diagrams of the open-loop system simulations and the wind-tunnel experiments at $U = 13.01$ m/s, (a) $h - \dot{h}$; (b) $\alpha - \dot{\alpha}$.

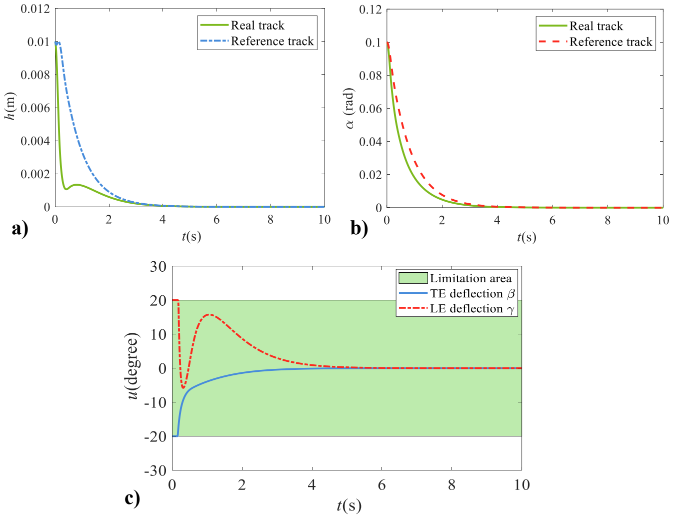

Fig. 7. Closed-loop responses with limited LE and TE control deflection at $U = 12$ m/s, (a) h ; (b) α ; and (c) β, γ ($u_{\max} = 20°$).

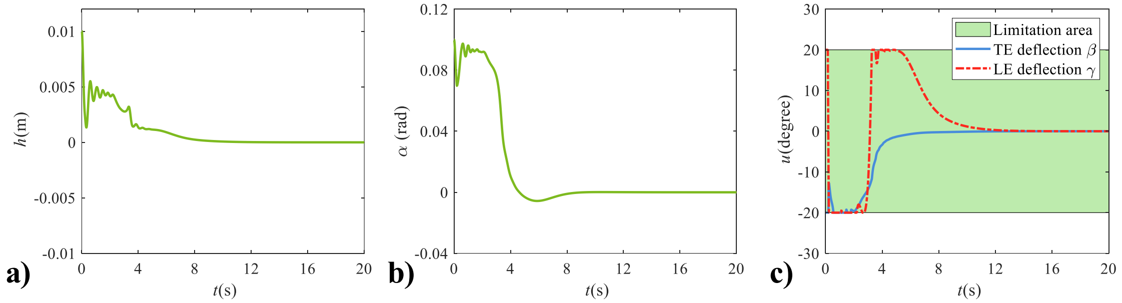

Fig. 8. Simulation results obtained by applying the control law reported in [49] to the present system at $U = 12$ m/s (with $g_1^{\mathrm{ref}} = 100, g_2^{\mathrm{ref}} = 10^8$ from [49]), (a) h ; (b) α ; and (c) β, γ ($u_{\max} = 20°$).

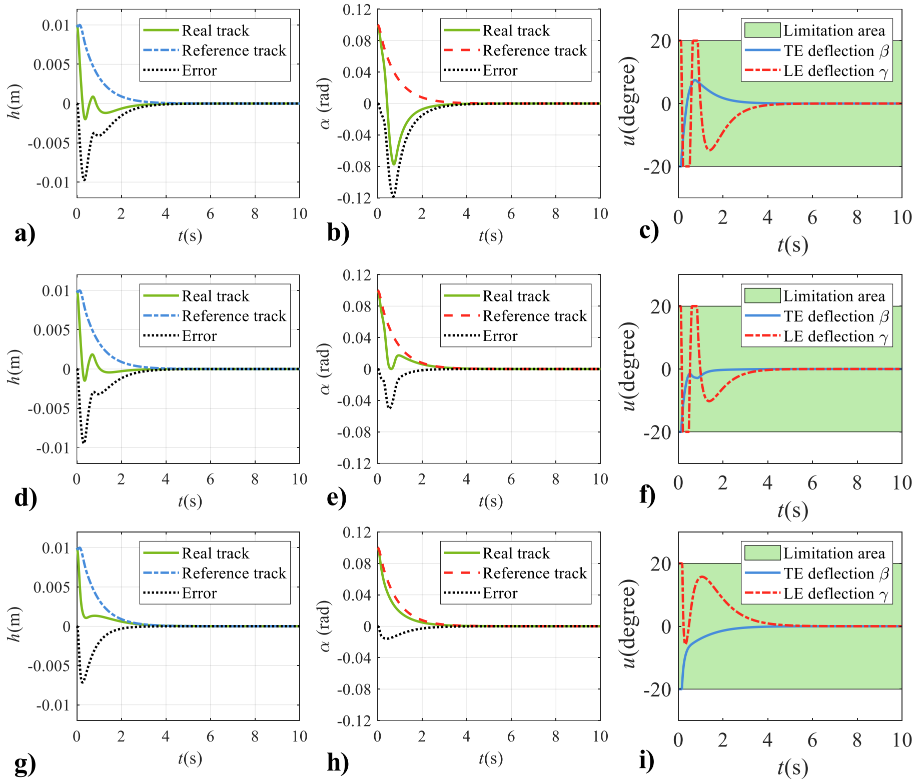

Fig. 9. Closed-loop responses for different gain matrices at $U = 12$ m/s, subfigures (a), (d), (g) h ; (b), (e), (h) α ; and (c), (f), (i) β, γ ($u_{\max} = 20°$).

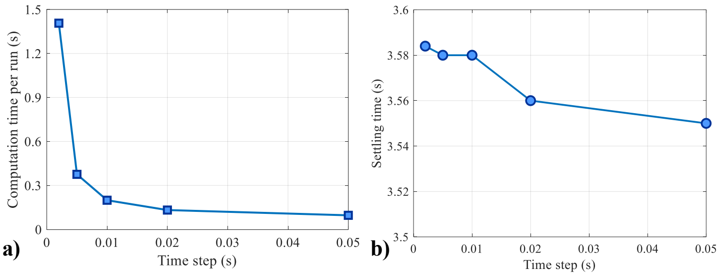

Fig. 10. Effect of time step on average computation time per run (a) and settling time (b).

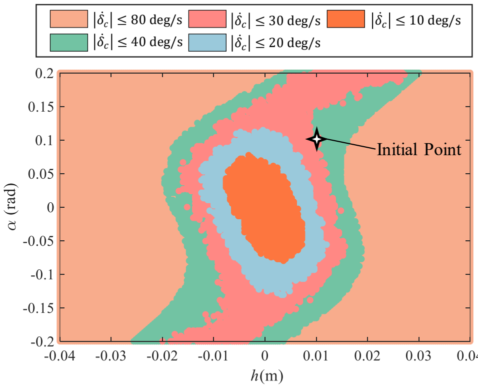

Fig. 11. Controllable region of the nonlinear system under $|\delta_c| \leq 20°$ and variable deflection rate constraints.

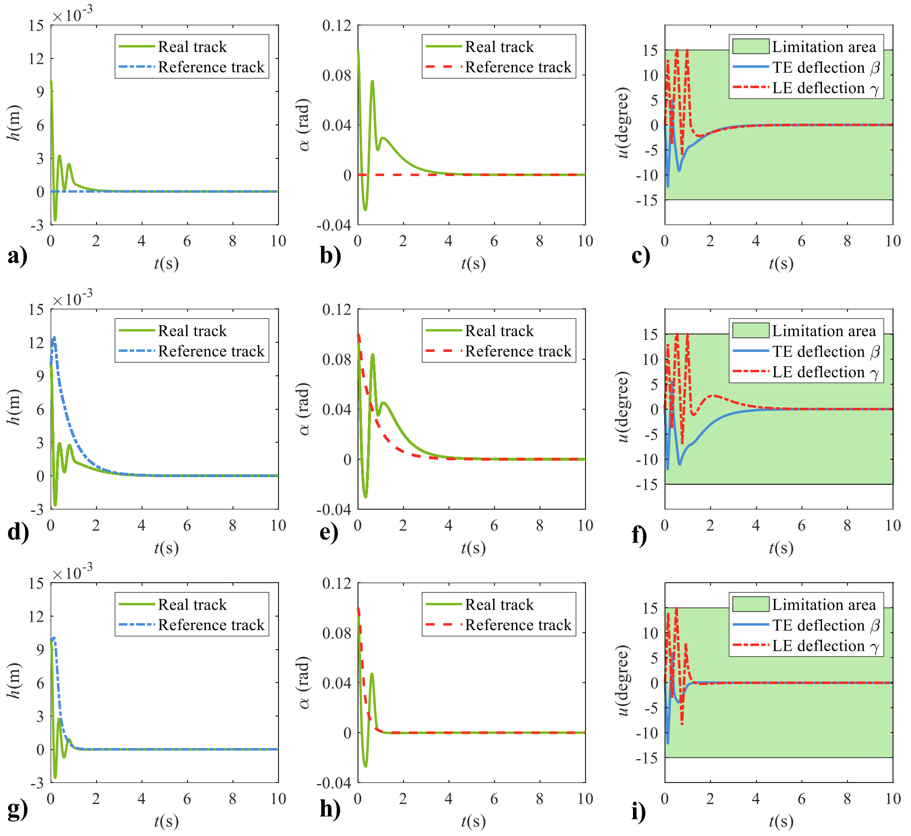

Fig. 12. Closed-loop responses for different reference trajectories at $U = 12$ m/s, subfigures (a), (d), (g) h ; (b), (e), (h) α ; and (c), (f), (i) β, γ ($|\delta_c| \leq 15°$, $|\dot{\delta}_c| \leq 100\,°/\mathrm{s}$).

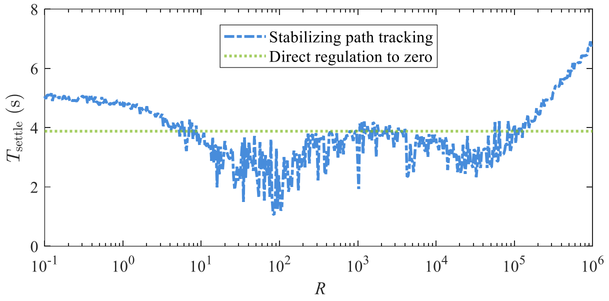

Fig. 13. Settling time for flutter suppression under different values of r_1

4.3 Comparative simulation of nonlinear stiffnesses

In the dynamic model of the real wing model, there exist various complex nonlinear forms [10], such as cubic nonlinearity, freeplay nonlinearity and coulomb nonlinearity. Thus, this section considers three different kinds of nonlinear pitch stiffness: quadratic, freeplay and piecewise constant stiffness. Fig. 14 shows the relation between stiffness k_α and pitch angle, which are expressed by

$$\begin{cases} k_{\alpha 1}^{*} = 12.77 + 53.47\alpha + 1003\alpha^{2}\ \mathrm{N \cdot m} \\ k_{\alpha 2}^{*} = \begin{cases} 50\ \mathrm{N \cdot m} & |\alpha| > 0.05\ \mathrm{rad} \\ 0\ \ \mathrm{N \cdot m} & |\alpha| \le 0.05\ \mathrm{rad} \end{cases} \\ k_{\alpha 3}^{*} = \begin{cases} 36\ \mathrm{N \cdot m} & |\alpha| > 0.05\ \mathrm{rad} \\ 10\ \ \mathrm{N \cdot m} & |\alpha| \le 0.05\ \mathrm{rad} \end{cases} \end{cases} \tag{48}$$

where the $k_{\alpha 1}^{*}$, $k_{\alpha 2}^{*}$ and $k_{\alpha 3}^{*}$ are quadratic, freeplay and piecewise constant pitch stiffness.

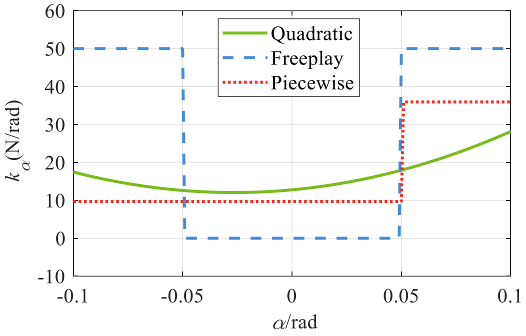

Fig. 14. Three nonlinear pitch stiffness $k_\alpha - \alpha$ curves.

In this section, the parameters of the $\boldsymbol{Q}$ and $\boldsymbol{R}$ matrices are selected with reference to Eq. (41). The feedback matrices are set as $\boldsymbol{g}_1 = Diag\{15,15\}$ and $\boldsymbol{g}_2 = Diag\{5,5\}$. For the same initial conditions as in Eq. (42), Fig. 15 shows the closed-loop system time response in plunge, pitch, LE, and TE deflection. It can be seen that the responses in plunging, pitching all decay to 0 within 6 s. In order to show the feasibility for different control situation, three stiffness models have been applied. They are quadratic stiffness, freeplay stiffness and piecewise constant stiffness, respectively. The settling times T_{settle} for the three different pitch stiffness model are given by

$$\begin{cases} T_{\text{settle}}^{\alpha 1} = 3.78\ \mathrm{s} \\ T_{\text{settle}}^{\alpha 2} = 3.94\ \mathrm{s} \\ T_{\text{settle}}^{\alpha 3} = 3.86\ \mathrm{s} \end{cases} \tag{49}$$

The settling times of the three models are all within 4 s. Although the free-play stiffness model is more challenging to control, all three are effectively stabilised by the inverse dynamic method and satisfy the flutter suppression requirement. These results confirm the capability of the inverse dynamic method in handling aeroelastic instability for 2-DOF wing systems with three different pitch stiffness. This method may also be extended to other nonlinear stiffness models.

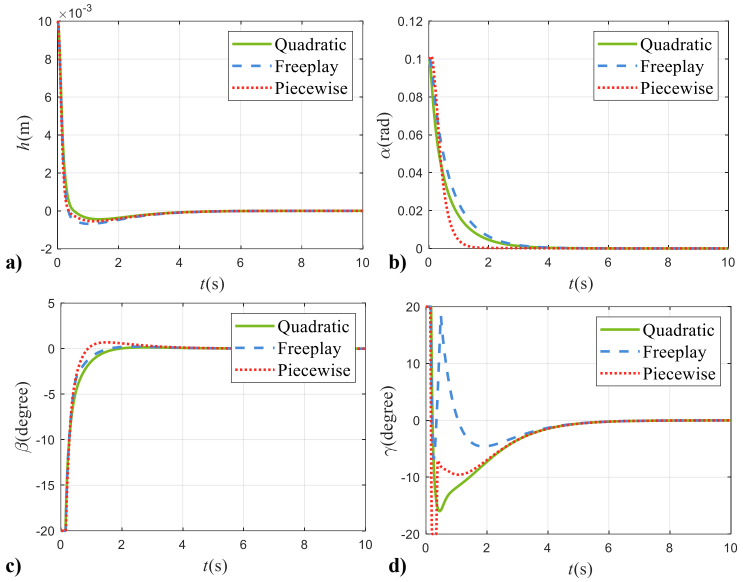

Fig. 15. Closed-loop responses of three pitch stiffness at $U = 12$ m/s, (a) h ; (b) α ; and (c) β and (d) γ ($u_{\max} = 20°$).

5 Model parameter uncertainty analysis

5.1 Uncertainty parameter selection and distribution characterization

The flutter problems in this aeroelastic system are challenging to quantitatively describe due to the uncertain parameters. These uncertainties have complex effects on the dynamics of the system. In this paper, the Monte Carlo method [50] is combined with numerical simulations to solve this problem. The effect of parameter uncertainty on the wing flutter velocity and the controllable boundary problem of the system have been further studied for the quadratic pitch stiffness model.

To simplify the uncertainty problem, it is assumed that some of the geometrical parameters, material properties and other parameters in the model obey a Gaussian distribution [12]. The initial value $\boldsymbol{C}_0$ of coefficients of variation $\boldsymbol{C}_v = [C_{v1}, \cdots, C_{v12}]^{\mathrm{T}}$ is tabulated in TABLE V [51], which is defined as

$$C_{vi} = \frac{\sigma_{p_i}}{\mu_{p_i}} \times 100\% \; (i = 1,2 \cdots 12) \tag{50}$$

where p_i denotes the system parameters listed in TABLE V: c_α, c_h, k_α, k_h, x_α, m_{W}, m_{T}, I_α, a, b, s, and ρ. Parameter C_{vi}, σ_{p_i}, and μ_{p_i} denote the coefficient of variation, standard deviation and mean value of parameter p_i, respectively. These parameters were selected because they represent independent physical quantities that can be directly measured or controlled during manufacturing, such as masses, dimensions, and stiffness coefficients. Most other aeroelastic parameters in the model are derived or normalized from these independent variables. Treating these fundamental quantities as the primary uncertainty sources captures variability at its origin and avoids introducing artificial correlations among parameters.

The coefficient of variation is closely related to the standard deviation and describe the extent of dispersion of a particular parameter. In general, a higher coefficient of variation corresponds to a higher degree of dispersion of the system data. The mean values and coefficients of variation of some of the parameters in the model are shown in TABLE V. Prior to system-wide uncertainty analysis, the effects of individual parameters on flutter velocity may be evaluated to quantify their sensitivity impacts. Simulations were conducted using the linear sampling method. For this nonlinear system, the regression-based sensitivity factors $\boldsymbol{C}_s = [C_{s1}, \cdots, C_{s12}]^{\mathrm{T}}$ are defined as follows:

$$C_{s_i} = \frac{\partial U_c(p_1, \cdots, p_{12})}{\partial p_i} \cdot \frac{\sigma_{p_i}}{\sigma_{U_c}} \times 100\% \; (i = 1,2 \cdots 12) \tag{51}$$

where $U_c = U_c(p_1, \cdots, p_{12})$ denotes the closed-loop flutter speed of the 2-DOF wing system, depending critically on 12 system parameters $p_1 - p_{12}$.

The computational results of parameter sensitivity are presented in TABLE V and Fig. 16. The computational results demonstrate that increasing plunge stiffness k_h, wingspan s, semi-chord b, and air density ρ reduces the closed-loop flutter speed of the system, thereby elevating the risk of flutter failure. Conversely, increasing pitching stiffness k_α, total mass m_{T}, and non-dimensional distance a elevates the closed-loop flutter speed, thereby enhancing system stability. The aforementioned sensitivity analyses may provide a guidance for wing design optimization, especially for parameters demonstrating strong coupling effects on flutter characteristics. It should be noted that, however, local sensitivity analysis quantifies parametric sensitivity to small variations around mean values. If the parameter variations are substantial, a global sensitivity analysis may be conducted.

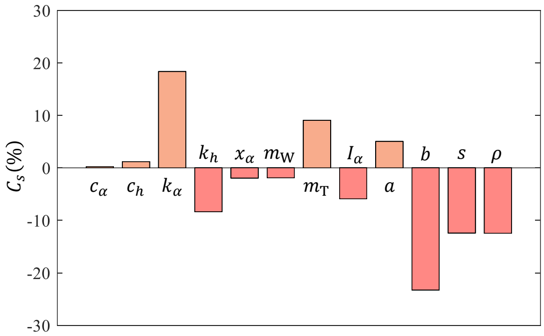

Fig. 16. Probabilistic sensitivity factors for 2-DOF wing section with nonlinear stiffness.

To investigate the effects of parameter uncertainties, closed-loop flutter velocity was computed via 1×10^4 random samples with stochastic uncertainties. Under simple random sampling, the sampled parameters p_1 to p_{12} follow Gaussian distributions. The sample standard deviation

$\sigma_i (i = 1,2 \cdots 12)$ is given by $\sigma_i = \mu_i C_{vi}$, where the mean value μ_i is shown in TABLE V. The initial state variables and the state feedback coefficients of the system are the same as in Fig. 7. Counting the number of the flutter in different freestream velocities, Fig. 17 (a) presents the histograms of the distributions of the flutter onset speed under $\boldsymbol{C}_v = \boldsymbol{C}_0$. The distribution of the flutter onset velocity is similar to the normal distribution. To ensure the stability of the closed-loop system, the flutter onset speed U_{c2} is defined as the controllable boundary at which the cumulative distribution function (CDF) curve reaches 0.1%. That is, when the freestream velocity is below this boundary, at least 9990 out of the 10000 Monte Carlo samples remain controllable. It should be noted that this boundary reflects a statistical screening result under finite-sample conditions and does not represent a deterministic safety limit. This threshold is a design choice rather than a universal criterion, and a more stringent value can be adopted for applications requiring higher reliability. At this freestream velocity U_{c2}, the flutter phenomenon occurs in only 0.1% of the 1×10^4 random samples. Thus, it is reliable to define U_{c2} as the flutter controllable boundary of the closed-loop system. The predicted controllable boundary of the system with uncertain parameters is shown in Fig. 17 (b). The controllable boundaries at $\boldsymbol{C}_v = \boldsymbol{C}_0$ is chosen as:

$$U_{c2} = 43.1 \text{ m/s} \ \ (\text{CDF} = 0.1\%;\ \boldsymbol{C}_v = \boldsymbol{c}_0) \tag{52}$$

TABLE V Uncertainty parameters of the 2-DOF wing section model

$\boldsymbol{p}$	$\boldsymbol{\mu}$	$\boldsymbol{C}_v$	$\boldsymbol{C}_s$
c_α	$0.0360\ \text{kg}\cdot\text{m}^2/\text{s}$	5%	0.23%
c_h	$27.43\ \text{kg/s}$	5%	1.17%
k_α	$k_\alpha(\alpha)$	4%	18.34%
k_h	$2844\ \text{N/m}$	3%	−8.35%
x_α	0.5721	2%	−1.93%
m_W	5.230 kg	0.2%	−1.90%
m_T	15.57 kg	0.2%	9.05%
I_α	$0.1419\ \text{kg}\cdot\text{m}^2$	4%	−5.89%
a	−0.6719	1%	5.02%
b	0.1905 m	0.2%	−23.26%
s	0.5945 m	0.2%	−12.40%
ρ	$1.225\ \text{kg/m}^3$	1.5%	−12.46%

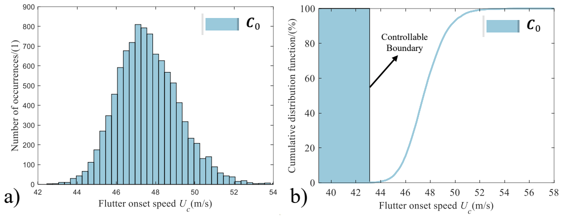

Fig. 17. Statistical results of the flutter onset speed at $\boldsymbol{C}_v = \boldsymbol{C}_0$, (a) number of flutter occurrences; (b) CDF of flutter occurrences and predicted controllable boundary ($u_{\max} = 20°$)

5.2 Effect of coefficient of variation on controllable boundary

In order to study the effect of $\boldsymbol{C}_v$ on the controllable boundary, the coefficient of variation is changed to $\mathbf{0}$, $0.5\boldsymbol{C}_0$ and $1.5\boldsymbol{C}_0$, respectively. The statistical results are presented in Fig. 18. When $\boldsymbol{C}_v$ decreases from $\boldsymbol{C}_0$ to $\mathbf{0}$, the closed flutter velocity can be written as

$$U_{c0} = 47.5 \text{ m/s} \ \ (\boldsymbol{C}_v = \mathbf{0}) \tag{53}$$

In addition, the controllable boundaries at $\boldsymbol{C}_v = 0.5\boldsymbol{C}_0$ and $\boldsymbol{C}_v = 1.5\boldsymbol{C}_0$ are expressed by

$$\begin{cases} U_{c1} = 45.2 \text{ m/s} \ \ (\text{CDF} = 0.1\%; \ \boldsymbol{C}_v = 0.5\boldsymbol{C}_0) \\ U_{c3} = 41.2 \text{ m/s} \ \ (\text{CDF} = 0.1\%; \ \boldsymbol{C}_v = 1.5\boldsymbol{C}_0) \end{cases} \tag{54}$$

It is clear that the different speeds satisfy the following size relationship.

$$U_{c0} > U_{c1} > U_{c2} > U_{c3} > U_0 = 9.8 \text{ m/s} \tag{55}$$

where the $U_0 = 9.8$ m/s is the open-loop flutter velocity of the nonlinear system.

The comparison shows that decreasing $\boldsymbol{C}_v$ can increase the controllable boundaries of the closed-loop system and vice versa. The critical flutter speed of the closed-loop system is increased by a factor of $4.20 - 4.61$ compared to the open-loop. For the parameter uncertainty problem of this quadratic nonlinear stiffness system, the controllable boundaries under different $\boldsymbol{C}_v$ are calculated by Monte Carlo method. These results confirm that the proposed control strategy maintains its efficacy in suppressing flutter for the 2-DOF wing system, even when subject to parameter uncertainties. In addition, we can also define a safe flight envelope, ensuring flutter avoidance with 99.9% probability.

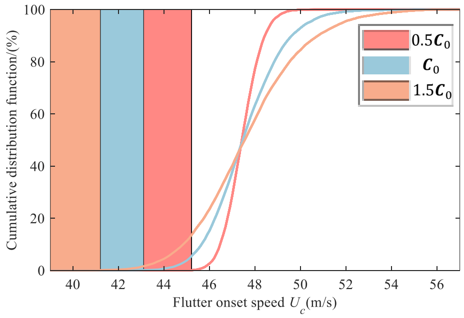

Fig. 18. The CDF of flutter occurrences and predicted controllable boundaries at different $\boldsymbol{C}_v$ ($u_{\max} = 20°$).

6 Gust alleviation

6.1 Modeling approach

The aeroelastic dynamic model with gust interference may consist of structure dynamic model and aerodynamic model. In this work, the former is a 2-DOF wing model with LE and TE control surfaces, as in Eq. (1). The latter needs to add gust loads on the basis of quasi-steady aerodynamic force and torque. In this problem, only the vertical gusts are considered for interference due to its effect on the effective angle of attack (AOA) of the wing system. The modelling approach of the aeroelastic model with gust interference is shown in Fig. 19. The inverse dynamic method may also be used for load alleviation in response to gust interference.

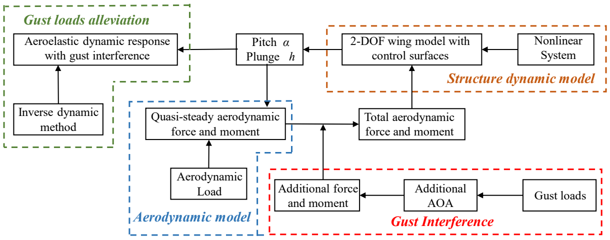

Fig. 19. The modeling approach of aeroelastic dynamic model with gust interference.

6.2 Gust velocity model and updating aeroelastic dynamic model

As for vertical gusts, the discrete gust model is a classically common form of the engineering gust disturbance [52]. It can be used to characterize discrete wind shear, peaks in atmospheric turbulence, and terrain-induced flows, among others. In gust experiments and simulations, only considering the vertical gust, the $1 - $cosine uniform gust [53] is commonly used and can be expressed by

$$w_{g1} = \begin{cases} \frac{W_g}{2}\left[1 - \cos\left(\frac{\pi U t}{L_g}\right)\right], 0 \le t \le T \\ 0, t < 0 \,\&\, t > T \end{cases} \tag{56}$$

Another common type of model is the continuous gust model, which is a power spectrum model obtained through theoretical and experimental studies of atmospheric turbulence phenomena. In this paper, the von Karman continuous gust model is used [53], which is more reflective of the turbulence characteristics of the atmosphere than the Dryden model [54]. According to the military specification [55], the power spectral density function is written as

$$\phi_w(\omega) = \frac{\sigma_w^2 \tau_w}{\pi} \cdot \frac{1 + \frac{8}{3}(1.339\omega\tau_w)^2}{[1 + (1.339\omega\tau_w)^2]^{\frac{11}{6}}} \tag{57}$$

Eq. (57) can be transformed to the time domain. As the power spectral density function is given, the generation of time-domain gust signals may be achieved via the superposition of sinusoidal functions [56]. The spatial domain turbulent velocity components can be expressed as

$$w_{g2}(x_g) = \sum_i A_i \sin(\Omega_i x_g + \theta_i) \tag{58}$$

where A_i is amplitudes of the i^{th} sine function of the w_{g2} functions, with magnitude governed by the power spectral density function. Ω_i and θ_i represent the spatial circular frequency and the random phase angle, respectively. x_g denotes the spatial variable, transformed into the time domain through the relation $x_g = Ut$. Gust velocities in the spatial domain $w_{g2}(x_g)$ can be converted to the time domain $w_{g2}(t)$ via the same relation $x_g = Ut$. Considering the effects of vertical gusts, Fig. 20 illustrates the updated aeroelastic dynamic model.

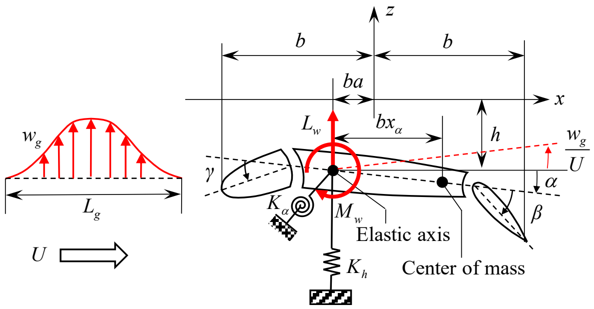

Fig. 20. 2-DOF wing model with gust interference.

Assuming that the vertical gust wind velocity is much less than the freestream velocity, (3) may be rewritten as

$$\begin{cases} L = \rho U^2 bsC_{l\alpha}\left[\alpha_w + (\dot{h}/U) + \left(\frac{1}{2} - a\right) b(\dot{\alpha}/U)\right] \\ \quad +\rho U^2 bsC_{l\beta}\beta + \rho U^2 bsC_{l\gamma}\gamma \\ M = \rho U^2 b^2 sC_{m\alpha-\mathrm{eff}}\left[\alpha_w + (\dot{h}/U) + \left(\frac{1}{2} - a\right) b(\dot{\alpha}/U)\right] \\ \quad +\rho U^2 b^2 sC_{m\beta-\mathrm{eff}}\beta + \rho U^2 b^2 sC_{m\gamma-\mathrm{eff}}\gamma \end{cases} \tag{59}$$

where L_w and M_w are the quasi-steady aerodynamic force and moment when the gust exists, and α_w is the effective AOA, which is defined as

$$\alpha_w = \alpha + \Delta\alpha = \alpha + \frac{w_g}{U} \tag{60}$$

The gust disturbance induces an effective AOA variation $\Delta\alpha$, which is superimposed on the nominal pitch angle α. This perturbation modifies the flow field, inducing transient lift fluctuations ΔL and pitching moments ΔM through altered pressure distribution on lifting surfaces. Eq. (3) may be replaced with (59) to obtain the new state space equation, and it is expressed by

$$\begin{cases}\dot{\boldsymbol{x}} = \boldsymbol{A}\boldsymbol{x} + \boldsymbol{B}\boldsymbol{u} + \boldsymbol{G}w_g \\ \boldsymbol{y} = \boldsymbol{C}\boldsymbol{x}\end{cases} \tag{61}$$

where $\boldsymbol{G}$ is the gust input matrix, given by

$$\boldsymbol{G} = \begin{bmatrix} -(\rho U b s C_{l\alpha} I_\alpha + m_{\mathrm{W}} x_\alpha \rho U b^3 s C_{m\alpha-\mathrm{eff}})/D \\ (m_{\mathrm{W}} x_\alpha \rho U b^2 s C_{l\alpha} + m_{\mathrm{T}} \rho U b^2 s C_{m\alpha-\mathrm{eff}})/D \\ 0 \\ 0 \end{bmatrix} \tag{62}$$

6.3 Gust alleviation by the inverse dynamic method

Similar to the flutter suppression control law design, the 2-DOF wing system state space may be rewritten as

$$\dot{\boldsymbol{x}} = \begin{bmatrix} \boldsymbol{A}_{11} & \boldsymbol{A}_{12} \\ \boldsymbol{E}_1 & \boldsymbol{O}_1 \end{bmatrix} \boldsymbol{x} + \begin{bmatrix} \boldsymbol{B}_{11} \\ \boldsymbol{O}_1 \end{bmatrix} \boldsymbol{u} + \begin{bmatrix} \boldsymbol{G}_1 \\ \boldsymbol{O}_1 \end{bmatrix} w_g \tag{63}$$

where the matrices $\boldsymbol{E}_1$, $\boldsymbol{O}_1$, $\boldsymbol{A}_{11}$, $\boldsymbol{A}_{12}$ and $\boldsymbol{B}_{11}$ are defined in (26). $\boldsymbol{G}_1$ is one part of gust input matrix, and is defined as

$$\boldsymbol{G}_1 = \begin{bmatrix} -(\rho U b s C_{l\alpha} I_\alpha + m_{\mathrm{W}} x_\alpha \rho U b^3 s C_{m\alpha-\mathrm{eff}})/D \\ (m_{\mathrm{W}} x_\alpha \rho U b^2 s C_{l\alpha} + m_{\mathrm{T}} \rho U b^2 s C_{m\alpha-\mathrm{eff}})/D \end{bmatrix} \tag{64}$$

The controller used in the gust alleviation analysis is identical to that developed for flutter suppression in Eq. (32). The gust is treated as an external random disturbance, and the controller structure remains unchanged. In this section, four different gust input conditions are considered to verify the gust alleviation effect of the inverse dynamic method. These four conditions are given in TABLE VI. For this 2-DOF wing model, the open-loop flutter velocity is $U_0 = 9.8\,m/s$. Thus, we select two velocities before and after the flutter to ensure the rigor of the simulation($U_1 = 9\ \mathrm{m/s} < U_0 < U_2 = 12\ \mathrm{m/s}$). The amplitude and the scale of the discrete gust are chosen as $W_g = 0.15U_j\ (j = 1, 2)$ and $L_g = 10$ m. These gust parameters are selected as illustrative values to demonstrate the feasibility of the proposed framework. They do not represent a specific flight condition or airworthiness requirement, and other parameter values can be accommodated without modifying the control structure. The time domain responses of the closed-loop system, subjected to gust disturbance, are shown from Fig. 21 to Fig. 24. The assessment of the inverse dynamic method to alleviate the gust is described by gust alleviation rate η, which is defined as

$$\eta = \frac{r_{open} - r_{closed}}{r_{open}} \times 100\% \tag{65}$$

where the r_{open} and r_{closed} are the root mean square (RMS) of state variable acceleration under open-loop and closed-loop conditions, respectively.

The alleviation efficacy of the control scheme acting on the RMS of acceleration is shown in TABLE VII. For condition 1, the inverse dynamic method has poor alleviation effect. However, compared to conditions 2 to 4, the RMS values in condition 1 are minimal and may not be affected on the motion smoothness of the 2-DOF wing system. Under this condition, the inverse dynamic method fails to effectively reduce the RMS of state variable acceleration. For conditions from 2 to 4, the control strategy has high efficiency with gust disturbance, achieving the alleviation rate of 75.59% – 95.68% compared to the open-loop. When the freestream velocity is greater than the open-loop flutter velocity, the acceleration responses in both discrete and continuous gust model decays to within 5% of the peak value within 3 seconds. Overall, the system acceleration responses under gust disturbances can be confined within a small range using the inverse dynamic method, demonstrating the potential of this approach for gust-induced acceleration alleviation.

TABLE VI Four different gust input cases of the 2-DOF wing section model

Condition	Freestream velocity	Gust model
1	$U_1 = 9\,\mathrm{m/s}$	Discrete
2	$U_1 = 9\,\mathrm{m/s}$	Continuous
3	$U_2 = 12\,\mathrm{m/s}$	Discrete
4	$U_2 = 12\,\mathrm{m/s}$	Continuous

TABLE VII The gust alleviation efficacy of the control scheme of the 2-DOF wing section model

Condition	RMS of plunge acceleration $(\mathrm{m/s^2})$		$\eta_h(\%)$	RMS of pitch acceleration$(\mathrm{rad/s^2})$		$\eta_\alpha(\%)$
	Open	Closed		Open	Closed	
1	0.0416	0.0162	61.01	0.5844	0.4088	30.05
2	0.3574	0.0575	83.90	5.5229	1.3480	75.59
3	0.9275	0.0578	93.77	30.9762	1.3393	95.68
4	1.2338	0.1049	91.50	41.3405	2.2062	94.66

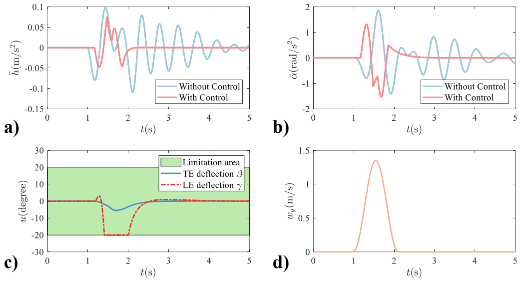

Fig. 21. Closed-loop responses with gust in condition 1, (a) $\ddot{h}$; (b) $\ddot{\alpha}$; (c) β, γ ($u_{\max} = 20°$) ; and (d) w_g.

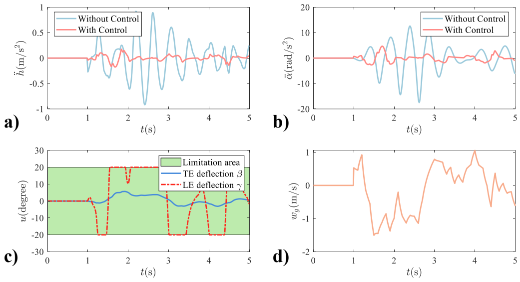

Fig. 22. Closed-loop responses with gust in condition 2, (a) $\ddot{h}$; (b) $\ddot{\alpha}$; (c) β, γ ($u_{\max} = 20°$) ; and (d) w_g.

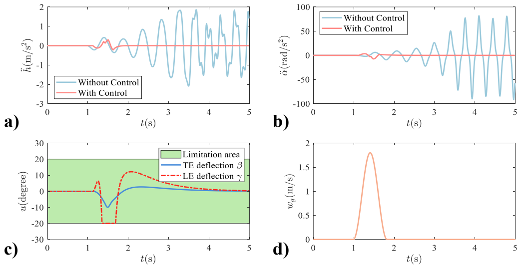

Fig. 23. Closed-loop responses with gust in condition 3, (a) $\ddot{h}$; (b) $\ddot{\alpha}$; (c) β, γ ($u_{\max} = 20°$) ; and (d) w_g.

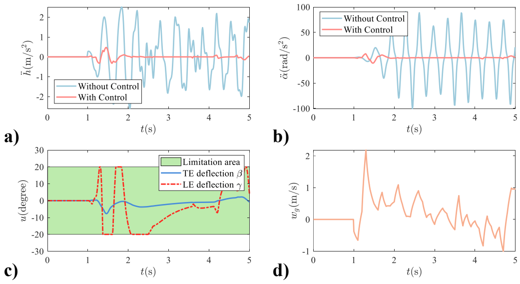

Fig. 24. Closed-loop responses with gust in condition 4, (a) $\ddot{h}$; (b) $\ddot{\alpha}$; (c) β, γ ($u_{\max} = 20°$) ; and (d) w_g.

7 Conclusions

This paper has introduced the concept of using the inverse dynamic method to suppress the flutter of a 2-DOF wing system with nonlinear pitch stiffness. The method is based on three main features:

explicit construction of a reference trajectory via linearization around the equilibrium and LQR method, direct cancellation of the nonlinear stiffness and quasi-steady aerodynamic terms through the inverse dynamics control law, and separate treatment of the nominal nonlinearity and parameter uncertainty.

The study begins by examining the open-loop flutter characteristics of this system and validating the model compared to previous experiments. The inverse dynamic method is then applied to control a 2-DOF wing section with nonlinear pitch stiffness in simulation. Under the stated assumptions, the tracking error is shown to converge asymptotically to zero via Lyapunov stability theory and LaSalle's invariance principle. When control surface saturation and rate constraints are present, the aerodynamic forces and moments generated may be insufficient to perfectly track the reference trajectory. Although this precludes global stability, the proposed strategy still ensures a considerable controllable region.

A parametric sensitivity analysis is also conducted to identify the parameters that most strongly influence the closed-loop flutter speed. In addition, to address uncertainties in the 2-DOF wing system, the Monte Carlo method is combined with numerical simulations to predict controllable boundaries. The effect of the coefficient of variation on the controllable boundary is also examined. Furthermore, a control strategy is implemented for gust disturbance, and the system acceleration responses are reduced to a small range. These results demonstrate that the proposed trajectory-based inverse dynamics framework is a viable approach for flutter suppression of a 2-DOF wing section with nonlinear pitch stiffness.

Future work should proceed in several directions. First, the quasi-steady aerodynamic model adopted in this study could be extended to incorporate unsteady aerodynamic effects, compressibility corrections, and dynamic stall models. This would allow a more accurate assessment of the control performance under conditions closer to practical flight. Second, the uncertainty quantification framework could be extended toward global sensitivity analysis and more rigorous robustness treatments. The inclusion of sensor noise, state estimation errors, and control loop time delay would further bridge the gap between the current numerical validation and practical implementation. Third, the RMS-based gust alleviation evaluation could be strengthened by incorporating additional metrics such as structural load alleviation rates and control energy consumption. The specific gust condition for which limited alleviation is observed also warrants further investigation. Finally, extending the proposed control strategy to three-dimensional wing configurations would allow spanwise aerodynamic effects to be considered and enable a more realistic assessment of its applicability to aircraft structures.

Acknowledgements This work was supported in part by the National Natural Science Foundation of China (Grant No. 12102017, 92271104), and in part by the Beijing Natural Science Foundation (Grant No. 1232014).

Author contributions J. Y. Zhang proposed the idea and its related contribution and novelties. He established the initial model framework and provided critical guidance throughout the work. C. X. Zhang was responsible for the related mathematical formulation and subsequent model development. He performed all simulations, analyzed and extracted the resulting data. He also wrote the original draft.

Data availability Data will be made available on request.

Declarations

Competing interests The authors declare no competing interests.

REFERENCES

[1] Theodorsen T (1935) General theory of aerodynamic instability and the mechanism of flutter. Report NASA No. 496
[2] Bisplinghoff RL, Ashley H, Halfman RL (1955) Aeroelasticity. Dover Publications, New York
[3] Livne E (2018) Aircraft active flutter suppression: state of the art and technology maturation needs. J Aircr 55(1):410–452
[4] Silva GC et al (2018) Active and passive control for acceleration reduction of an aeroelastic typical wing section. J Vib Control 24(13):2673–2687
[5] Burnett EL et al (2016) Design and flight test of active flutter suppression on the X-56A multi-utility technology test-bed aircraft. Aeronaut J 120(1228):893–909
[6] Cheng P, Wang Y (2010) Fundamentals of modern control theory. Beihang University Press, Beijing
[7] Zou Q, Huang R, Hu H (2022) Body-freedom flutter suppression for a flexible flying-wing drone via time-delayed control. J Guid Control Dynam 45(1):28–38
[8] Sinou J-J (2022) Flutter instability and active aeroelastic control with time delay for a two-dimensional airfoil. Eur J Mech Solid 92:104465
[9] Ouyang Y et al (2021) Active flutter suppression of wing with morphing flap. Aerosp Sci Technol 110:106457
[10] Chen YS (2021) Nonlinear vibration. Higher Education Press, Beijing
[11] Panchal J, Benaroya H (2021) Review of control surface freeplay. Prog Aerosp Sci 127:100729
[12] Li Y, Yang ZC (2010) Uncertainty quantification in flutter analysis for an airfoil with preloaded freeplay. J Aircr 47(4):1454–1457
[13] Wu S, Livne E (2017) Alternative aerodynamic uncertainty modeling approaches for flutter reliability analysis. AIAA J 55(8):2808–2823
[14] Qiang X, Wang C, Zhang H (2026) Interval theory-embedded data-driven identification framework for uncertain thermo-elastic parameters. Appl Math Model 155:116743
[15] Xie C, Zhu L, An C, Shao Y (2025) A rapid steady/unsteady aerodynamic analysis method based on panel method coupled boundary layer theory. Aerosp Sci Technol 165:110494
[16] Yang Q, Teng W, Guo K, Wang T, Zhao L, Hui Y, Liu M (2026) Large eddy simulation of self-excited forces in forced-vibration square prisms: lock-in regime dynamics and vortex shedding modulation. J Wind Eng Ind Aerod 270:106338
[17] Li YH, Qin N (2022) A review of flow control for gust load alleviation. Appl Sci 12(20):10537
[18] Wu Z, Cao Y, Ismail M (2019) Gust loads on aircraft. Aeronaut J 123(1266):1216–1274
[19] Gong W, Zhang Y, Zhu M, Chen T, Zheng Z (2025) Dynamic control of multiple stratospheric airships in time-varying wind fields for communication coverage missions. Aerosp Sci Technol 166:110514
[20] Guo D, Zhang Z, Liu J, Zhang J, Lin Y (2026) Multi-horizon flight trajectory prediction enabled by time-frequency wavelet transform. Nat Commun 17:633
[21] Seghour L, Tatar N-E, Berkani A (2020) Stability of a thermoelastic laminated system subject to a neutral delay. Math Methods Appl Sci 43:285–303
[22] Berkani A (2018) Stabilization of a viscoelastic rotating Euler-Bernoulli beam. Math Methods Appl Sci 41:2939–2960

[23] Berkani A, Tatar N-E, Khemmoudja A (2017) Control of a viscoelastic translational Euler–Bernoulli beam. Math Methods Appl Sci 40:237–254
[24] Berkani A, Tatar N-E, Khemmoudja A (2018) Vibration control of a viscoelastic translational Euler-Bernoulli beam. J Dyn Control Syst 24:167–199
[25] Jalalian SA, Tourajizadeh H, Hosseini SAA (2025) Modelling and nonlinear control of aircraft wings flutter by use of piezoelectric patch considering the airfoil shape cross section of the wing beam. Nonlinear Dyn 113:25429–25458
[26] Li D et al (2021) Observer-based sliding mode control for piezoelectric wing bending-torsion coupling flutter involving delayed output. J Vib Control 27(15–16):1824–1841
[27] Patartics B et al (2022) Application of structured robust synthesis for flexible aircraft flutter suppression. IEEE Trans Control Syst Technol 30(1):311–325
[28] Gao Z, Li Y, Liu H (2018) Fault-tolerant control for wing flutter under actuator faults and time delay. J Vib Eng Technol 6:429–439
[29] Schmidt DK et al (2020) Modeling, design, and flight testing of three flutter controllers for a flying-wing drone. J Aircr 57(4):615–634
[30] Downs PS, Prazenica RJ (2023) Adaptive control of a flexible wing for flutter suppression and disturbance rejection. AIAA SCITECH 2023 Forum, National Harbor, MD & ONLINE
[31] Mozaffari-Jovin S, Firouz-Abadi RD, Roshanian J (2024) L1 adaptive aeroelastic control of an unsteady flapped airfoil in the presence of unmatched nonlinear uncertainties. J Sound Vib 578:118334
[32] Chen G, Sun J, Li YM (2023) Optimized disturbance rejection control for flutter suppression of a benchmark active control technology wind-tunnel model. In: Proceedings of the 2022 International Conference on Applied Nonlinear Dynamics, Vibration and Control (Lecture Notes in Electrical Engineering, vol 952). Springer, Singapore, pp 3861–3871
[33] Yang ZJ et al (2017) Design of an active disturbance rejection control for transonic flutter suppression. J Guid Control Dynam 40(11):2905–2916
[34] Yang ZJ et al (2019) Transonic flutter suppression for a three-dimensional elastic wing via active disturbance rejection control. J Sound Vib 445:168–187
[35] Ebrahimzadeh N, Dardel M, Shafaghat R (2021) Modeling and control design for flutter suppression using active dynamic vibration absorber. J Vib Eng Technol 9:845–860
[36] Li S, Wang S, Zhang Y, Wang X, Zhang Y, Wu W, Chen R, Mu R (2026) Distributed bearing-based fault-tolerant formation control of fixed-wing UAV swarm with prescribed performance. Aerosp Sci Technol 168:110897
[37] Xiong J-J, Wang X-Y, Li C (2025) Recurrent neural network based sliding mode control for an uncertain tilting quadrotor UAV. Int J Robust Nonlinear Control 35:8030–8046
[38] Wang G, Feng Z, Qu Y, Sun H (2025) Event-triggered adaptive predefined-time anti-unwinding attitude tracking control for spacecraft. PLoS One 20(10):e0333700
[39] Mclnnes CR (1998) Satellite attitude slew manoeuvres using inverse control. Aeronaut J 102(1015):259–266
[40] Zhang JY, Mclnnes CR (2015) Reconfiguring smart structures using approximate heteroclinic connections. Smart Mater Struct 24:105034
[41] Armoon M et al (2022) Robust inverse dynamics control of the remotely operated underwater vehicle manipulator. In: 2022 8th International Conference on Control, Instrumentation and Automation (ICCIA), Tehran, Iran, Islamic Republic
[42] Nie B et al (2021) Design and validation of disturbance rejection dynamic inverse control for a tailless aircraft in wind tunnel. Appl Sci 11(4):1407
[43] Zhang Z, Zhang K, Han Z (2024) Incremental nonlinear dynamic inverse-adaptive sliding mode three-dimensional angle constrained guidance law design. IEEE Trans Aerosp Electron Syst 60(1):186–201
[44] Min C et al (2023) Trajectory optimization of an electric vehicle with minimum energy consumption using inverse dynamics model and servo constraints. Mech Mach Theory 181:105185
[45] Platanitis G, Strganac TW (2004) Control of a nonlinear wing section using leading- and trailing-edge surfaces. J Guid Control Dynam 27(1):52–58
[46] Gallardo-Alvarado J, Gallardo-Razo J (2022) Linear algebra. Academic Press, Pittsburgh
[47] Li DC, Xiang JW, Guo SJ (2011) Adaptive control of a nonlinear aeroelastic system. Aerosp Sci Technol 15(5):343–352
[48] Rekik M et al (2024) LHS-GA based H-infinity control for robust airfoil flutter suppression. IEEE Access 12:171500–171512
[49] Lee KW, Singh SN (2022) Composite adaptive control and identification of MIMO aeroelastic system with enhanced parameter excitation. J Aerosp Eng 35(6):04022093
[50] Hu ZW, Zhang BQ, Yang J (2020) A two-phase Monte Carlo simulation/non-intrusive polynomial chaos (MSC/NIPC) method for quantification of margins and mixed uncertainties (QMMU) in flutter analysis. IEEE Access 8:118773–118786

[51] Hughes WJ (2015) Aeroelastic variability and uncertainty of composite aircraft. FAA ANG-E2, Washington, DC, USA, Rep. DOT/FAA/TC-15/19
[52] Ahmadi M, Farsadi T, Khodaparast HH (2024) Enhancing gust load alleviation performance in an optimized composite wing using passive wingtip devices: folding and twist approaches. Aerosp Sci Technol 147:109023
[53] Cavaliere D, Fezans N (2024) Toward automated gust load alleviation control design via discrete gust impulse filters. J Guid Control Dynam 47(4):697–710
[54] Wang LJ et al (2019) A comparative study of gust load alleviation of UAV based on LPV and MPC controller. In: 2019 Chinese Control Conference (CCC), Guangzhou, China
[55] Anon (1980) Military specification, flying qualities of piloted airplanes. USA, MIL-F-8785C
[56] Beal TR (1993) Digital simulation of atmospheric turbulence for Dryden and von Karman models. J Guid Control Dynam 16(1):132–138

Chenxi Zhang was born in Shandong, China, in 2001. He is currently studying toward the Master's degree in mechanical engineering in Beihang University His research interests include, nonlinear control, flutter and wing vibration control.

Jiaying Zhang received the Ph.D. degree in mechanical and aerospace engineering from the University of Strathclyde, Glasgow, UK, in 2018. He is currently a Professor in Beihang University. His current research interests include nonlinear dynamic and control, morphing aircraft system.